J|A|C|S
ARTICLES
Published on Web 05/09/2006

The Properties of the $[Mn_{12}O_{12}(O_2CR)_{16}(H_2O)_4]$ Single-Molecule Magnets in Truly Axial Symmetry: $[Mn_{12}O_{12}(O_2CCH_2Br)_{16}(H_2O)_4]\cdot 4CH_2Cl_2$

Nicole E. Chakov,[†] Sheng-Chiang Lee,[‡] Andrew G. Harter,[§] Philip L. Kuhns,[§] Arneil P. Reyes,[§] Stephen O. Hill,[‡] N. S. Dalal,[§] Wolfgang Wernsdorfer,[⊥] Khalil A. Abboud,[†] and George Christou*[,†]

Contribution from the Department of Chemistry, University of Florida, Gainesville, Florida 32611, Department of Physics, University of Florida, Gainesville, Florida 32611, Department of Chemistry and Biochemistry, and National High Magnetic Field Laboratory, Florida State University, Tallahassee, Florida 32306, and Laboratoire Louis Néel-CNRS, BP 166, 25 Avenue des Martyrs, 38042, Grenoble, Cedex 9, France

Received February 8, 2006; E-mail: christou@chem.ulf.edu

Abstract: Detailed studies are reported of a Mn_{12} single-molecule magnet (SMM) in truly axial (tetragonal) symmetry. The complex is $[Mn_{12}O_{12}(O_2CCH_2Br)_{16}(H_2O)_4]\cdot 4CH_2Cl_2$ (**2**·$4CH_2Cl_2$ or Mn_{12}−BrAc), obtained by the standard carboxylate substitution method. The complex has an $S = 10$ ground state, typical of the Mn_{12} family, and displays frequency-dependent out-of-phase AC susceptibility signals and hysteresis in single-crystal magnetization vs applied DC field sweeps. Single-crystal high-frequency EPR spectra in frequencies up to 360 GHz exhibit narrow signals that are not overlapping multiplets, in contrast to $[Mn_{12}O_{12}(O_2CMe)_{16}(H_2O)_4]\cdot 2MeCO_2H\cdot 4H_2O$ (**1** or Mn_{12}−Ac), which also crystallizes in an axial (tetragonal) space group but which now is recognized to consist of a mixture of six hydrogen-bonded isomers in the crystal and thus gives multiple, inhomogeneously broadened EPR signals. Similarly, single-crystal ^{55}Mn NMR spectra on Mn_{12}−BrAc display much sharper signals than a single crystal of Mn_{12}−Ac, and this allows one Mn^{III} signal to show an almost baseline-resolved quintet from quadrupolar splitting (^{55}Mn, $I = 5/2$, 100%), allowing quadrupole coupling parameters (e^2qQ) to be determined. In addition, it was found that crushing crystals of Mn_{12}−BrAc into a microcrystalline powder causes severe broadening and shifts of the NMR resonances, emphasizing the superiority of single-crystal studies. The combined results establish that Mn_{12}−BrAc is far superior to Mn_{12}−Ac for the study of the intrinsic properties of the Mn_{12} family of SMMs in axial symmetry, and for the search for new phenomena such as quantum interference effects caused by higher-order (>2nd-order) transverse terms in the spin Hamiltonian.

Introduction

Single-molecule magnets (SMMs) are individual molecules that function as nanoscale magnetic particles.[1−3] They derive their properties from the combination of a large ground-state spin quantum number (S) and a magnetoanisotropy of the easy-axis or Ising-type (negative zero-field splitting parameter, D). This combination leads to a significant barrier (U) to relaxation (reorientation) of the magnetization vector, whose maximum value is given by $S^2|D|$ or $(S^2 - {}^1/_4)|D|$ for integer and half-integer spin, respectively. Experimentally, a SMM shows superparamagnet-like properties, exhibiting both a frequency-dependent out-of-phase AC magnetic susceptibility, and hysteresis in a plot of magnetization vs applied DC magnetic field. SMMs thus represent a molecular (or bottom-up) approach to nanoscale magnetism, and they are consequently also referred to occasionally as molecular nanomagnets. In addition, they clearly straddle the classical/quantum interface, displaying not just the classical property of magnetization hysteresis but also the quantum properties of quantum tunneling of the magnetization (QTM)[4] through the anisotropy barrier, and quantum phase interference.[5]

The first and still best studied SMMs are the mixed-valent $[Mn_{12}O_{12}(O_2CR)_{16}(H_2O)_4]$ (Mn_{12}; R = various) family with an $S = 10$ ground state, which are the SMMs with the highest blocking temperatures and thus the ones that have attracted the

[†] Department of Chemistry, University of Florida.
[‡] Department of Physics, University of Florida.
[§] Department of Chemistry and Biochemistry, and National High Magnetic Field Laboratory, Florida State University.
[⊥] Laboratoire Louis Néel-CNRS.

(1) (a) Sessoli, R.; Tsai, H.-L.; Schake, A. R.; Wang, S.; Vincent, J. B.; Folting, K.; Gatteschi, D.; Christou, G.; Hendrickson, D. N. *J. Am. Chem. Soc.* **1993**, *115*, 1804. (b) Sessoli, R.; Gatteschi, D.; Caneschi, A.; Novak, M. A. *Nature* **1993**, *365*, 141.
(2) Christou, G.; Gatteschi, D.; Hendrickson, D. N.; Sessoli, R. *MRS Bull.* **2000**, *25*, 66.
(3) Christou, G. *Polyhedron*, **2005**, *24*, 2065.
(4) Friedman, J. R.; Sarachik, M. P.; Tejada, J.; Ziolo, R. *Phys. Rev. Lett.* **1996**, *76*, 3830.
(5) (a) Wernsdorfer, W.; Sessoli, R. *Science* **1999**, *284*, 133. (b) Wernsdorfer, W.; Soler, M.; Christou, G.; Hendrickson, D. N. *J. Appl. Phys.* **2002**, *91*, 7164. (c) Wernsdorfer, W.; Chakov, N. E.; Christou, G. *Phys. Rev. Lett.* **2005**, *95*, 037203 (1−4).

most study by many groups around the world. The first example of a Mn_{12} SMM was the R = Me derivative $[Mn_{12}O_{12}(O_2CMe)_{16}(H_2O)_4]\cdot 2MeCO_2H\cdot 4H_2O$ (**1**).[1,6] This compound crystallizes in the tetragonal space group *I*4(*bar*) with the molecules all parallel and lying on an S_4 symmetry axis. The ease of preparation of this complex, coupled with its highly crystalline nature and high-symmetry space group, which simplifies the spin Hamiltonian by precluding second-order transverse (rhombic) terms, i.e., $E(\hat{S}_x^2 - \hat{S}_y^2)$ (E is the rhombic zero-field-splitting (ZFS) parameter), has made **1** the favorite for detailed study by a myriad of techniques. This was true even though many other Mn_{12} derivatives had since been obtained in crystalline form, almost always crystallizing in triclinic or monoclinic space groups with lower molecular site-symmetry than axial.[7]

It has, however, now become apparent that rather than **1** being a paragon of a Mn_{12} SMM, it is instead a mixture of six isomers differing in the number n (n = 0−4) of OH···O hydrogen-bonding interactions with the lattice $MeCO_2H$ molecules of crystallization,[8−15] with only two of these isomers (n = 0 and 4) possessing S_4 symmetry. Many previous studies on **1** have thus involved studies of a mixture of species,[16−23] and the obtained data will have been affected by this to various extents, depending on the technique. In some cases, such as the use of a sensitive technique such as EPR, this manifests itself as inhomogeneously broadened[16−21] and even multiple signals corresponding to the various isomers.[8,9,11−14] Of course, "one does not know what one is missing until one finds it", and it was only the recent studies with sensitive techniques (EPR, NMR) on new Mn_{12} derivatives with tetragonal symmetry, and no mixture of isomers, that finally provided an inkling of the high quality data that can be obtained for Mn_{12} in truly axial symmetry and with essentially no distributions of molecular environments in the crystal.[13,24−26]

Two such new and axially symmetric Mn_{12} complexes have been under detailed study by us recently: the R = $BrCH_2$[13,24] and R = Bu^tCH_2[13,26] derivatives. It is the purpose of this paper to describe in full the results from the detailed studies that we have recently been carrying out on the former, complex **2**, by a variety of techniques to document the properties of Mn_{12} complexes in truly axial symmetry. This will also clearly emphasize how superior are these data to those of complex **1**, and thus displace the latter as the benchmark within this field. The described techniques include X-ray diffraction, various magnetization and magnetic susceptibility studies, as well as hysteresis, high-frequency EPR, and ^{55}Mn NMR studies, all on single crystals.

Experimental Section

Synthesis. All manipulations were performed under aerobic conditions using materials as received, except where otherwise noted. $[Mn_{12}O_{12}(O_2CMe)_{16}(H_2O)_4]\cdot 2MeCO_2H\cdot 4H_2O$ (**1**) was prepared as described elsewhere.[1,6]

$[Mn_{12}O_{12}(O_2CCH_2Br)_{16}(H_2O)_4]$ (2). To a solution of complex **1** (2.0 g, 0.97 mmol) in a mixture of MeCN (50 cm^3) and CH_2Cl_2 (50 cm^3) was added $BrCH_2CO_2H$ (4.3 g, 31 mmol). The mixture was stirred for 1 h, and the solvent was then removed in vacuo. Toluene (20 cm^3) was added to the residue, and the solution was again evaporated to dryness. The addition and removal of toluene was repeated two more times. The remaining solid was redissolved in CH_2Cl_2 (75 cm^3) and treated again with $BrCH_2CO_2H$ (4.3 g, 31 mmol). After 1 h, three more cycles of addition and removal of toluene were performed. The residue was redissolved in CH_2Cl_2 (100 cm^3) and filtered. Hexanes (25 cm^3) were added, and the solution was allowed to stand undisturbed at room temperature for 4 days. The resulting black crystals were collected by filtration, washed with hexanes, and dried in vacuo; yield 96%. A sample for crystallography was maintained in contact with the mother liquor to prevent the loss of interstitial solvent. Dried solid analyzed as solvent-free. Anal. Calcd (found) for **2** ($C_{32}H_{40}Mn_{12}O_{48}Br_{16}$): C, 12.77 (12.84); H, 1.10 (1.01); N, 0.00 (0.00). Selected IR data (cm^{-1}): 1720 (w), 1597 (vs), 1574 (vs), 1557 (s), 1534 (s), 1419 (vs), 1402 (vs), 1359 (s), 1209 (m), 1116 (w), 958 (w), 896 (w), 733 (m), 680 (s), 645 (s), 603 (s), 553 (s), 525 (m).

X-ray Crystallography. Data were collected using a Siemens SMART PLATFORM equipped with a CCD area detector and a graphite monochromator utilizing Mo K_α radiation (λ = 0.71073 Å). A suitable single crystal of **2**·4CH_2Cl_2 was attached to a glass fiber using silicone grease and transferred to the goniostat where it was cooled to −100 °C for characterization and data collection. The structure was solved by direct methods (SHELXTL)[27] and standard Fourier techniques and was refined using full-matrix least-squares methods. All non-hydrogen atoms were refined anisotropically. Hydrogen atoms were placed in calculated positions and refined with the use of a riding model. Cell parameters were refined using up to 8192 reflections. A full sphere of data (1850 frames) was collected using the ω-scan method (0.3° frame width). The first 50 frames were remeasured at the end of data collection to monitor instrument and crystal stability (maximum

(6) Lis. T. *Acta Crystallogr*. **1980**, *B36*, 2042.
(7) (a) Eppley, H. J.; Tsai, H.-L.; de Vries, N.; Folting, K.; Christou, G.; Hendrickson, D. N. *J. Am. Chem. Soc.* **1995**, *117*, 301. (b) Artus, P.; Boskovic, C.; Yoo, J.; Streib, W. E.; Brunel, L.-C.; Hendrickson, D. N.; Christou, G. *Inorg. Chem.* **2001**, *40*, 4199. (c) Soler, M.; Artus, P.; Folting, K.; Huffman, J. C.; Hendrickson D. N.; Christou, G. *Inorg. Chem.* **2001**, *40*, 4902. (d) Chakov, N. E.; Abboud, K. A.; Zakharov, L. N.; Rheingold, A. L.; Hendrickson, D. N.; Christou, G. *Polyhedron*, **2003**, *22*, 1759. (e) Brockman, J. T.; Abboud, K. A.; Hendrickson D. N.; Christou, G. *Polyhedron*, **2003**, *22*, 1765. (f) Soler, M.; Wernsdorfer, W.; Sun, Z.; Ruiz, D.; Huffman, J. C.; Hendrickson, D. N.; Christou, G. *Polyhedron*, **2003**, *22*, 1783.
(8) Cornia, A.; Sessoli, R.; Sorace, L.; Gatteschi, D.; Barra, A. L.; Daiguebonne, C. *Phys. Rev. Lett.* **2002**, *89*, 257201.
(9) Hill, S.; Edwards, R. S.; Jones, S. I.; Dalal, N. S.; North, J. M. *Phys. Rev. Lett.* **2003**, *90*, 217204.
(10) del Barco, E.; Kent, A. D.; Rumberger, E. M.; Hendrickson, D. N.; Christou, G. *Phys. Rev. Lett.* **2003**, *91*, 047203.
(11) Takahashi, S.; Edwards, R. S.; North, J. M.; Hill, S.; Dalal, N. S. *Phys. Rev. B* **2004**, *70*, 094429.
(12) del Barco, E.; Kent, A. D.; Hill, S.; North, J. M.; Dalal, N. S.; Rumberger, E. M.; Hendrickson, D. N.; Chakov, N. E.; Christou, G. *J. Low Temp. Phys.* **2005**, *140*, 119.
(13) Hill, S.; Anderson, N.; Wilson, A.; Takahashi, S.; Petukhov, K.; Chakov, N. E.; Murugesu, M.; North, J. M.; del Barco, E.; Kent, A. D.; Dalal, N. S.; Christou, G. *Polyhedron*, **2005**, *24*, 2284.
(14) Park, K.; Baruah, T.; Bernstein, N.; Pederson, M. R.; *Phys. Rev. B* **2004**, *69*, 144426.
(15) Bircher, R.; Chaboussant, G.; Sieber, A.; Güdel, H. U.; Mutka, H. *Phys. Rev. B* **2004**, *70*, 212413.
(16) Maccagnano, S.; Achey, R.; Negusse, E.; Lussier, A.; Mola, M. M.; Hill, S.; Dalal, N. S. *Polyhedron*, **2001**, *20*, 1441.
(17) Parks, B.; Loomis, J.; Rumberger, E.; Hendrickson, D. N.; Christou, G.; *Phys. Rev. B* **2001**, *64*, 184426.
(18) Park, K.; Novotny, M. A.; Dalal, N. S.; Hill, S.; Rikvold, P. A. *Phys. Rev. B* **2002**, *65*, 014426.
(19) Park, K.; Novotny, M. A.; Dalal, N. S.; Hill, S.; Rikvold, P. A. *Phys. Rev. B* **2002**, *66*, 144409.
(20) Hill, S.; Maccagnano, S.; Park, K.; Achey, R. M.; North, J. M.; Dalal, N. S. *Phys. Rev. B* **2002**, *65*, 224410.
(21) Chudnovsky, E. M.; Garanin, D. A. *Phys. Rev. Lett.* **2001**, *87*, 187203.
(22) Mertes, K. M.; Suzuki, Y.; Sarachik, M. P.; Paltiel, Y.; Shtrikman, H.; Zeldov, E.; Rumberger, E.; Hendrickson, D. N.; Christou, G.; *Phys. Rev. Lett.* **2001**, *87*, 227205.
(23) del Barco, E.; Kent, A. D.; Rumberger, E. M.; Hendrickson, D. N.; Christou, G.; *Europhys. Lett.* **2002**, *60* (5), 768.
(24) Petukhov, K.; Hill, S.; Chakov, N. E.; Abboud, K. A.; Christou, G. *Phys. Rev. B* **2004**, *70*, 054426.
(25) (a) Harter, A. G.; Chakov, N. E.; Roberts, B.; Achey, R.; Reyes, A.; Kuhns, P.; Christou, G.; Dalal, N. S. *Inorg. Chem.* **2005**, *44*, 2122. (b) Harter, A. G.; Chakov, N. E.; Roberts, B.; Achey, R.; Reyes, A.; Kuhns, P.; Christou, G.; Dalal, N. S. *Polyhedron* **2005**, *24*, 2346.
(26) Wernsdorfer, W.; Murugesu, M.; Christou, G. *Phys. Rev. Lett.* **2006**, *96*, 057208.
(27) Sheldrick, G. M. *SHELXTL5*. Bruker-AXS: Madison, Wisconsin, 1998.

Table 1. Crystallographic Data for **2**·$4CH_2Cl_2$

parameter	**2**·$4CH_2Cl_2$
formula[a]	$C_{36}H_{48}Cl_8Mn_{12}Br_{16}O_{48}$
fw, g mol^{-1}	3470.09
space group	$I4_1/a$
a, Å	26.9948(16)
b, Å	26.9948(16)
c, Å	12.7245(11)
V, Å^3	9272.6(11)
Z	4
T, °C	−100(2)
radiation, Å[b]	0.71073
ρ_{calc}, g cm^{-3}	2.480
μ, cm^{-1}	87.86
R1 (wR2), %[c,d]	5.68 (15.43)

[a] Including solvent molecules. [b] Graphite monochromator. [c] $R1 = \sum||F_o| - |F_c||/\sum|F_o|$. [d] $wR2 = [\sum[w(F_o^2 - F_c^2)^2]/\sum[wF_o^2)^2]]^{1/2}$ where $S = [\sum[w(F_o^2 - F_c^2)^2]/(n - p)]^{1/2}$, $w = 1/[\sigma^2(F_o^2) + (m\cdot p)^2 + n\cdot p]$, $p = [\max(F_o^2,0) + 2F_c^2]/3$, and m and n are constants.

correction on I was <1%). Absorption corrections by integration were applied based on measured indexed crystal faces.

An initial survey of reciprocal space revealed a set of reflections with a tetragonal lattice. Analysis of the full data set revealed that the space group was $I4_1/a$. The asymmetric unit contains one-quarter of the Mn_{12} molecule and one disordered CH_2Cl_2 molecule. Bromine atoms Br(2) and Br(3) in two of the $BrCH_2CO_2^-$ ligands were slightly disordered about two positions; their site occupancies were each dependently refined to 94:6%. A more complex disorder was observed for Br(4) where seven possible positions for the atom were located, and the seven occupancies refined to a sum of 1.0. The disorder of Br(4) was coupled as a result of proximity with a disordered CH_2Cl_2 molecule of crystallization. The CH_2Cl_2 molecule was disordered over three positions and was refined using a model involving one C atom and two Cl atoms, each disordered over three positions. Three possible positions for each Cl atom were located, and the occupancies of the three atoms refined to a sum of 1.34 and 0.75 for Cl(1) and Cl(2), respectively. The corresponding C atom disorder could not be resolved. A total of 321 parameters were refined in the final cycle of refinement using 3860 reflections with $I > 2\sigma(I)$ to yield $R1$ and $wR2$ of 5.68 and 15.43%, respectively. The final difference Fourier map was essentially featureless, the largest peak being 1.905 e Å^{-3}, and the deepest hole being −1.185 e Å^{-3}.

The crystallographic data and structure refinement details are collected in Table 1.

DC and AC Magnetometry. Variable-temperature DC magnetic susceptibility data down to 1.80 K were collected on a Quantum Design MPMS-XL SQUID magnetometer equipped with a 70 kG (7 T) DC magnet at the University of Florida. Pascal's constants were used to estimate the diamagnetic corrections, which were subtracted from the experimental susceptibility to give the molar magnetic susceptibility (χ_M). Samples were embedded in solid eicosane, unless otherwise stated, to prevent torquing. AC magnetic susceptibility data were collected on the same instrument, employing a 3.5 G field oscillating at frequencies up to 1500 Hz. Magnetization vs field and temperature data were fit using the program MAGNET, and contour plots were obtained using the program GRID, both written at Indiana University by E. R. Davidson.[28] Low-temperature (<1.8 K) hysteresis loop and DC relaxation studies were performed at Grenoble using an array of micro-SQUIDS.[29] The high sensitivity of this magnetometer allows the study of single crystals of SMMs of the order of 10−500 μm. The field can be applied in any direction by separately driving three orthogonal coils.

High-Frequency Electron Paramagnetic Resonance (HFEPR) Spectroscopy. HFEPR measurements were performed at various frequencies in the 50−360 GHz range. Single-crystal spectra were obtained at fixed microwave frequencies and temperatures using a sensitive cavity-perturbation technique, and a Millimeter-wave Vector Network Analyzer (MVNA) was employed as a source and detector (this instrumentation is described in detail elsewhere).[30,31] Hard-plane, angle-dependent measurements were performed in a 7 T horizontal field magnet with a vertical access. This setup also allows rotation about an orthogonal axis using a rotating cavity,[11,31] thereby enabling measurements with the field parallel to the magnetic easy-axis of the sample. The hard-plane measurements were performed at the fundamental TE011 mode of the cavity (51.3 GHz), and the sample was positioned optimally in the cavity for these studies. The higher-frequency measurements were performed on higher-order modes of the cavity. With the exception of one measurement, all samples were handled identically with a view to avoiding solvent loss from the structure. The needle-shaped single crystals (∼1.5 × 0.4 × 0.4 mm^3) were removed directly from their mother liquor and protected with grease before cooling under 1 atm of helium gas; the crystals were exposed to air for no more than a few seconds, and they were then cooled below 270 K within minutes of removal from the mother liquor.

^{55}Mn Nuclear Magnetic Resonance (NMR) Spectroscopy. Crystals of **2**·$4CH_2Cl_2$ of suitable dimensions for single-crystal studies (1.0 × 1.0 × 1.5 mm^3, the c-axis being parallel to the long face of the crystals) were obtained over a period of 1−4 weeks by slow evaporation of CH_2Cl_2 solutions of **2**, containing also a small amount of hexanes. A bulk solution of **2** (0.25 g) and $BrCH_2CO_2H$ (0.5 g) in CH_2Cl_2 (15 cm^3) was filtered and placed in many small vials. A small amount of hexanes was mixed into each solution and a plastic cap with a small hole in the top placed on each vial; the vials were left undisturbed at room temperature. Resulting crystals of suitable size were coated in fast-setting epoxy to allow for easier manipulation of the brittle material and to help prevent damage from thermal cycling. Aligned, microcrystalline powder samples were created by crushing crystals into a fine powder, which was mixed with Stycast 1266 epoxy, and the mixture was left overnight in a magnetic field of ∼8.5 T at a temperature of ∼295 K to align the crystallites.

NMR coils for both the single crystal and powder samples were made by wrapping Cu wire directly around the encapsulated samples. The single crystal was aligned in the coil such that the c-axis (easy axis) was perpendicular to the H_1 field produced by the coil. The probe used for zero-field frequency scans was inductively matched and could be tuned over a large range, 200−400 MHz, without having to adjust the matching. Because the breadth of the signal was so large, scans could take anywhere from 3 h to 1 day. Utilizing a stepper motor controlled by the spectrometer to aid in tuning greatly increased the efficiency of this process. The spectrometer, a MagRes 2000, was home-built with quadrature detection. $\pi/2-\pi/2$ pulse sequences were utilized for frequency scanning and spin−lattice relaxation time (T_1) measurements, with pulse times ranging from 500 to 1500 ns. Low-temperature T_1 studies were conducted with a Janis ^{3}He system; T_1 was measured over a 0.365−1.5 K range with the coil mounted such that it was in thermal contact with a brass plate touching the thermometer and heater.

Other Studies. Infrared spectra were recorded in the solid state (KBr pellets) on a Nicolet Nexus 670 FTIR spectrophotometer in the 400−4000 cm^{-1} range. Elemental analyses (C, H, N) were performed at the in-house facilities of the University of Florida Chemistry Department. Electrochemical studies were performed under argon using a BAS model CV-50W voltammetric analyzer and a standard three-electrode assembly (glassy carbon working, Pt wire auxiliary, and Ag/Ag_3I_4 reference) with 0.1 M $NBu^n_4PF_6$ as supporting electrolyte. No IR compensation was employed. Quoted potentials are versus the ferrocene/ferrocenium couple, used as an internal standard. The scan rates for cyclic voltammetry (CV) and differential pulse voltammetry (DPV)

(28) (a) Davidson, E. R. *MAGNET*; Indiana University: Bloomington, IN, 1999. (b) Davidson, E. R. *GRID*; Indiana University: Bloomington, IN, 1999.
(29) Wernsdorfer, W. *Adv. Chem. Phys.* **2001**, *118*, 99.
(30) Mola, M.; Hill, S.; Goy, P.; Gross, M. *Rev. Sci. Instrum.* **2000**, *71*, 186.
(31) Takahashi, S.; Hill, S. *Rev. Sci. Instrum.* **2005**, *76*, 023114.

were 100 and 20 mV/s, respectively. Distilled solvents were employed, and the concentrations of the complexes were approximately 1 mM. Solution ^{1}H NMR spectra were obtained at 300 MHz on a Varian VXR-300 spectrometer, using protio-solvent signals as internal references.

Results and Discussion

Synthesis. Our previous development of efficient methods for the substitution of all the acetate groups of readily available $[Mn_{12}O_{12}(O_2CMe)_{16}(H_2O)_4]\cdot 2MeCO_2H\cdot 4H_2O$ (**1**, Mn_{12}−Ac) with essentially any other carboxylate of choice opened up access to a large family of Mn_{12} derivatives.[1,7,32−34] This has provided many advantages, including the ability to modify solubilities, redox potentials, crystallinity, and other properties of interest. In the present work, we have employed this ligand substitution procedure in a $MeCN/CH_2Cl_2$ solvent mixture to introduce $BrCH_2CO_2^-$ groups onto the Mn_{12} core. The preparation of **2** (Mn_{12}−BrAc) is summarized in eq 1.

$$[Mn_{12}O_{12}(O_2CMe)_{16}(H_2O)_4] + 16\ BrCH_2CO_2H \rightarrow [Mn_{12}O_{12}(O_2CCH_2Br)_{16}(H_2O)_4] + 16\ MeCO_2H \quad (1)$$

The ligand substitution reaction is an equilibrium that must be driven to completion by (i) using a carboxylic acid with a lower pK_a than that of acetic acid (4.76) and/or (ii) using an excess of $BrCH_2CO_2H$ and/or (iii) removing the acetic acid as its toluene azeotrope. In fact, we used all three of these conditions, employing an excess of $BrCH_2CO_2H$ (pK_a = 2.90)[35] and carrying out multiple cycles of addition and then removal of toluene under dynamic vacuum to remove acetic acid as its toluene azeotrope (28:72%; bp 101 °C at one atmosphere). This procedure successfully led to the isolation and crystallization of pure $[Mn_{12}O_{12}(O_2CCH_2Br)_{16}(H_2O)_4]$ (**2**) in nearly quantitative yield (∼96%). Crystallization from CH_2Cl_2/hexanes gave dark-brown crystals of **2**·4CH_2Cl_2 suitable for X-ray crystallography and other single-crystal studies described below. Note that this Mn_{12} derivative had also been prepared previously by others,[36a,b] who similarly used our ligand-substitution procedure starting with complex **1**. These previous workers also obtained the crystal structures of their products, but without locating and refining the CH_2Cl_2 solvent of crystallization. Since the Mn_{12} molecular environments are crucial to the present story, we have repeated the crystal structure of **2**·4CH_2Cl_2, and targeted the location and refinement of the CH_2Cl_2 molecules.

Electrochemistry. Electrochemical studies on various Mn_{12} complexes have revealed that they have a rich redox chemistry involving several oxidation and reduction processes, the $E_{1/2}$ potentials of which are very sensitive to the electron-withdrawing or -donating ability of the carboxylate R group.[7,32] Electron-withdrawing substituents shift the reduction potentials to chemically accessible values and have led to the successful isolation, crystallization, and characterization of both the one- and two-electron reduced Mn_{12} species.[7,32,34,37] The cyclic voltammogram (CV) and differential pulse voltammogram (DPV) of **2** are typical of the Mn_{12} family of complexes (see Supporting Information). There are two quasi-reversible reduction waves at 0.57 and 0.21 V vs ferrocene. Standard electrochemical criteria for quasi-reversible electron transfer, including CV peak separations, anodic/cathodic peak current ratio, and DPV peak broadness, are fulfilled by each redox process. A study of the scan rate (υ) dependence of each reduction process established a linear peak current (i_p) vs $\upsilon^{1/2}$ relationship, as predicted by the Randles−Sevcik equation for a diffusion-controlled process. This is shown in eq 2,

$$i_p = (2.687 \times 10^5) n^{3/2} \upsilon^{1/2} D^{1/2} A C \quad (2)$$

where n is the number of electrons in the half-reaction, A is the electrode area, and D and C are the diffusion coefficient and concentration, respectively, of the analyte. As expected, the $E_{1/2}$ values of the first and second reduction processes are shifted to more positive values than those of **1** (0.18 and −0.06 V, respectively). They are also very similar to those of the chloroacetate Mn_{12} derivative (0.60 and 0.30 V), as expected on the basis of the similarity of the pK_a values of $ClCH_2CO_2H$ (2.85) and $BrCH_2CO_2H$ (2.90).[35]

Description of Structure. A labeled ORTEP[38] plot in PovRay format of complex **2** is presented in Figure 1 (top), and a stereopair is provided in Supporting Information. Selected bond distances and angles are listed in Table 2. Complex **2**·4CH_2Cl_2 crystallizes in the tetragonal space group $I4_1/a$ with the Mn_{12} molecule located on a crystallographic S_4 improper rotation axis perpendicular to the disklike plane. For the sake of brevity, references to specific atoms in the following discussion implicitly include their symmetry-related partners. The complex has the same structure as previously characterized $[Mn_{12}O_{12}(O_2CR)_{16}(H_2O)_4]$ complexes,[1,34] possessing a central $[Mn^{IV}{}_4O_4]^{8+}$ cubane unit held within a nonplanar ring of eight Mn^{III} ions by eight μ_3-O^{2-} ions. The eight Mn^{III} ions separate into two groups of four each: Mn(2) is coordinated to a single Mn^{IV} ion via two oxide bridges, while Mn(1) is coordinated to two Mn^{IV} ions via two oxide bridges. Peripheral ligation is provided by 16 bridging $BrCH_2CO_2^-$ and four water molecules, O(1), which are bound in a 1:1:1:1 fashion, i.e., one each to the four Mn^{III} ions Mn(1), as required by the S_4 axis and as also found in **1**.

All of the Mn atoms are six-coordinate with near-octahedral geometry. The Mn oxidation levels were determined by charge considerations and inspection of Mn−O bond distances at each Mn. These assignments were confirmed quantitatively by bond valence sum (BVS)[39] calculations, indicating that Mn(1) and Mn(2) are Mn^{III} and the remaining Mn center, Mn(3), is Mn^{IV}. The eight Mn^{III} centers exhibit a Jahn−Teller (JT) distortion, as expected for a high-spin d^4 ion in near-octahedral geometry. As is almost always the case for Mn^{III} ions, the JT distortion is an axial elongation, typically of ∼0.1−0.2 Å for Mn−O bonds.

(32) Soler, M.; Wernsdorfer, W.; Abboud, K. A.; Huffman, J. C.; Davidson, E. R.; Hendrickson, D. N.; Christou, G. *J. Am. Chem. Soc.* **2003**, *125*, 3576.
(33) Eppley, H. J.; Christou, G. *Inorg. Synth.* **2002**, *33*, 61.
(34) Chakov, N. E.; Soler, M.; Wernsdorfer, W.; Abboud, K. A.; Christou, G. *Inorg. Chem.* **2005**, *44*, 53041.
(35) Rappoport, Z., Ed. *Tables for Organic Compound Identification*; CRC Press: Cleveland, OH, 1967.
(36) (a) Tsai, H.-L.; Chen, D.-M.; Yang, C.-I.; Jwo, T.-Y.; Wur, C.-S.; Lee, G.-H.; Wang, Y. *Inorg. Chem. Commun.* **2001**, *4*, 511. (b) An, J.; Chen, Z.-D.; Zhang, X.-X.; Raubenheimer, H. G.; Esterhuysen, C.; Gao, S.; Xu, G.-X. *Dalton Trans.* **2001**, *22*, 3352. (c) Bian, G.-Q.; Kuroda-Sowa, T.; Gunjima, N.; Maekawa, M.; Munakata, M. *Inorg. Chem. Commun.* **2005**, *8*, 208.
(37) Soler, M.; Chandra, S. K.; Ruiz, D.; Huffman, J. C.; Hendrickson, D. N.; Christou, G. *Polyhedron* **2001**, *20*, 1279.
(38) (a) Johnson, C. K.; Burnett, M. N. *ORTEP-III*, Report ORNL-6895: Oak Ridge National Laboratory: TN, 1996. (b) Farrugia, L. J. *J. Appl. Crystallogr.* **1997**, *30*, 565.
(39) (a) Brown, I. D.; Altermatt, D. *Acta Crystallogr.* **1985**, *B41*, 244. (b) Palenik, G. J. *Inorg. Chem.* **1997**, *36*, 4888. (c) Palenik, G. J. *Inorg. Chem.* **1997**, *36*, 122.

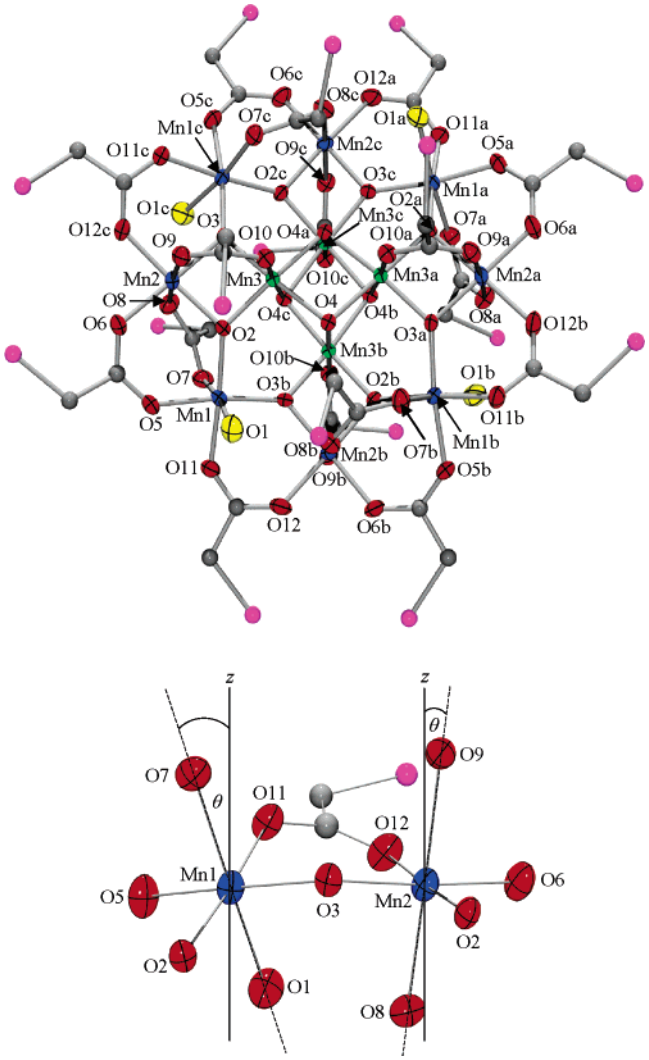

Figure 1. ORTEP representations in PovRay format: (top) complex **2** at the 50% probability level (except for the C and Br atoms), with the hydrogen atoms omitted for clarity; (bottom) the anisotropy (Jahn−Teller) axes (jagged lines) of Mn(1) and Mn(2), where θ is the angle of the local Mn^{III} anisotropy axis with respect to the crystallographic *z* axis. Mn^{IV} green; Mn^{III} blue; O red; H_2O yellow; Br pink; C gray.

The JT elongation axes all avoid the $Mn-O^{2-}$ bonds, the shortest and strongest in the molecule, and thus are all axially disposed, roughly perpendicular to the $[Mn_{12}O_{12}]$ disklike core. Complex **2**·4CH_2Cl_2 thus contains no abnormally oriented JT axes and is therefore the normal, common type of Mn_{12} Jahn−Teller isomer. This type of isomerism is defined as the occurrence of molecules that differ only in the orientation of one or more JT elongation axes,[40−42] and for Mn_{12} this is seen as a JT axis that is equatorial, pointing toward a core O^{2-} ion.

The precise orientation (θ) of each JT axis relative to the molecular *z* (S_4) axis (Figure 1, bottom) will be of relevance to the ^{55}Mn NMR spectroscopic studies and analyses to be described (vide infra), and these data are therefore provided here. The JT axes at Mn(1) and Mn(2) are at angles of $\theta = 34.0°$ and 7.9°, respectively; for these calculations, the Mn^{III} JT axes are defined by the O···O vector between the two trans Mn−O bonds.

Table 2. Selected Bond Distances (Å) and Angles (deg) for **2**·4CH_2Cl_2

parameter	**4**·4CH_2Cl_2
$Mn^{IV}-O_c$ (ax)	1.902(4)
$Mn^{IV}-O_c$ (eq)	1.922(4), 1.934(4)
$Mn^{IV}-O_r$	1.865(4), 1.878(4)
$Mn^{IV}-O_{ax}$	1.923(4)
$Mn^{IIIb}-O_r$	1.871(4), 1.902(4)
$Mn^{IIIc}-O_r$	1.898(4), 1.898(4)
$Mn^{IIIb}-O_{eq}$	1.932(5), 1.948(5)
$Mn^{IIIc}-O_{eq}$	1.959(4), 1.970(5)
$Mn^{IIIb}-O_{ax}$	2.187(5), 2.220(5)
$Mn^{IIIc}-O_{ax}$	2.114(5)
$Mn^{IIIc}-O_w$	2.193(5)
$O_r-Mn^{IV}-O_r$	83.75(17)
$O_r-Mn^{IIIb}-O_r$	82.91(17)
$O_r-Mn^{IIIc}-O_r$	92.35(17)
$Mn^{IV}\cdots Mn^{IV}$	2.8180(14), 2.8180(14), 2.9851(16)
$Mn^{IIIb}\cdots Mn^{IIIc}$	3.332, 3.388
$Mn^{IIIb}\cdots Mn^{IV}\cdots Mn^{IV}$	119.24(5), 121.28(5) 177.25(4)
$Mn^{IIIb}\cdots Mn^{IV}$	2.7938(12)
$Mn^{IIIc}\cdots Mn^{IV}$	3.460(2), 3.461(2)

[a] O_c = cubane O^{2-}, O_r = ring O^{2-}, O_{ax} = axial carboxylate, O_{eq} = equatorial carboxylate, O_w = water. [b] Mn^{III} atom Mn(2). [c] Mn^{III} atom Mn(1).

Location of the CH_2Cl_2 solvate molecules allows us to assess intermolecular contacts involving them, and we conclude there is evidence for only very weak intermolecular interactions. The only significant hydrogen-bonds are those between each bound water atom O(1) and Cl(4) of a CH_2Cl_2 molecule (O(1)···Cl(4) = 3.214 Å), but there is no corresponding HO···Cl hydrogen-bond between this CH_2Cl_2 and a second Mn_{12} molecule. Thus, the solvate molecules do not provide a hydrogen-bonding pathway for intermolecular exchange interactions. In addition, since each bound H_2O group is interacting with a separate CH_2Cl_2 molecule and there are four CH_2Cl_2 molecules per Mn_{12}, the hydrogen-bonding contacts do not serve to lower the local site symmetry from S_4 to any significant extent (i.e., other than the disorder in the CH_2Cl_2 orientations).

There are intermolecular Br(8)···Br(8) separations between neighboring molecules of 3.487 Å, slightly shorter than the sum of their van der Waals radii (3.70 Å),[43] but even this may be an artifact of the disorder over seven sites of the $BrCH_2CO_2^-$ ligand involved in this interaction; the site occupancy of position Br(8) is only 19%. It is thus concluded that there are at best only weak intermolecular contacts between separate Mn_{12} molecules, and that the stronger OH···Cl hydrogen bonds that are present neither bridge separate Mn_{12} molecules nor have other than a minimal symmetry-lowering effect on the local S_4 site-symmetry of each Mn_{12} molecule. This is in stark contrast to the situation in complex **1**, where (i) there are stronger OH···O hydrogen bonds between the Mn_{12} molecule and the lattice $MeCO_2H$ groups; (ii) there are only two $MeCO_2H$ groups per Mn_{12}, although each Mn_{12} is surrounded by four such groups in the tetragonal *I*4(*bar*) lattice; and (iii) depending on the orientation

(40) (a) Sun, Z.; Ruiz, D.; Dilley, N. R.; Soler, M.; Ribas, J.; Folting, K.; Maple, M. B.; Christou, G.; Hendrickson, D. N. *Chem. Commun.* **1999**, *19*, 1973. (b) Aubin, S. M. J.; Sun, Z.; Eppley, H. J.; Rumberger, E. M.; Guzei, I. A.; Folting, K.; Gantzel, P. K.; Rheingold, A. L.; Christou, G.; Hendrickson, D. N. *Inorg. Chem.* **2001**, *40*, 2127. (c) Aubin, S. M. J.; Sun, Z.; Eppley, H. J.; Rumberger, E. M.; Guzei, I. A.; Folting, P. K.; Gantzel, P. K.; Rheingold, A. L.; Christou, G.; Hendrickson, D. N. *Polyhedron* **2001**, *20*, 1139.
(41) Soler, M.; Wernsdorfer, W.; Sun, Z.; Huffman, J. C.; Hendrickson, D. N. Christou, G. *Chem. Commun.* **2003**, *21*, 2672.
(42) Zhao, H.; Berlinguette, C. P.; Basca, J.; Prosvirin, A. V.; Bera, J. K.; Tichy, S. E.; Schelter, E. J.; Dunbar, K. R. *Inorg. Chem.* **2004**, *43*, 1359.
(43) Bondi, A. *J. Phys. Chem.* **1964**, *68*, 441.

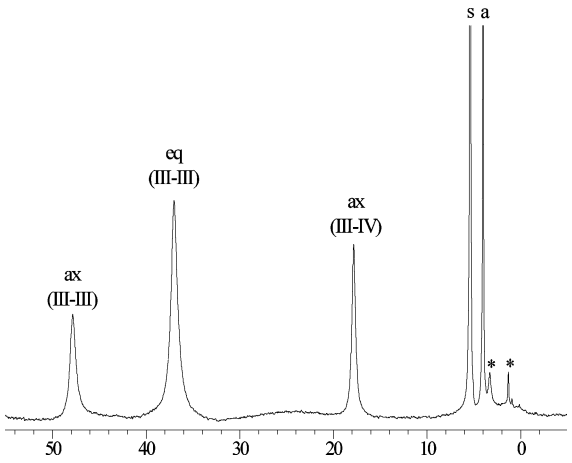

Figure 2. ^{1}H NMR (300 MHz) spectra at ~23 °C in CD_2Cl_2 solution of **2**. * are solvent impurities; s is the solvent protio-impurity; a is the $BrCH_2CO_2H$ protio-impurity.

Table 3. Solution ^{1}H NMR Spectral Data for Complex **2** in CD_2Cl_2

peak[a]	assignment[b]	T_1[c]
47.8	ax (III−III)	2.9
37.0	eq (III−III)	3.1
17.8	ax (III−IV)	5.1

[a] ppm, at ~23 °C. [b] ax = axial, eq = equatorial; III−III and III−IV refer to the ligand bridging a $Mn^{III}Mn^{III}$ and $Mn^{III}Mn^{IV}$ pair, respectively. [c] ms.

of a $MeCO_2H$ group, it can hydrogen bond with either of two neighboring Mn_{12} molecules.[8] As a consequence of these facts, crystals of **1** are a mixture of six Mn_{12} isomers, differing in the number n ($n = 0-4$) of $MeCO_2H$ groups to which they are hydrogen-bonded, with the $n = 2$ case also comprising cis and trans dispositions of the two $MeCO_2H$ groups. Only the $n = 0$ and 4 cases have local axial symmetry, and thus these different hydrogen-bonded forms represent a mixture of Mn_{12} molecules with a range of local symmetries. This will be crucial to understanding many of the observed differences between Mn_{12}−Ac (**1**) and Mn_{12}−BrAc (**2**) to be described below.

Solution ^{1}H NMR Spectroscopy. To assess the stability of complex **2** in solution, an NMR spectroscopic investigation was carried out in CD_2Cl_2. ^{1}H (and ^{19}F) NMR spectroscopy has only occasionally been used in the past to investigate the behavior in solution of $[Mn_{12}O_{12}(O_2CR)_{16}(H_2O)_4]^z$ ($z = 0$, 1−, and 2−) complexes.[7,32,34] Mn^{III} has a relatively fast electron relaxation time, and thus its electron relaxation cannot facilitate nuclear relaxation as efficiently as Mn^{II}, for example, making the Mn^{III} ion generally suitable for NMR spectroscopic study. The ^{1}H NMR spectrum of complex **2** in CD_2Cl_2 is shown in Figure 2, and chemical shifts and T_1 times are listed in Table 3. The isotropic shifts of the resonances are expected to have both contact (through-bond) and dipolar (through-space) contributions.[44] The spectrum exhibits three resonances with a 1:2:1 integration ratio. The S_4 axial symmetry of the Mn_{12} molecule yields four types of carboxylate groups in a 1:1:1:1 ratio, but as seen previously for other Mn_{12} derivatives, there is a fluxional process involving the axial water and one type of axial carboxylate group (the one that has both its O atoms located on the JT elongation axes of the $Mn^{III}\cdots Mn^{III}$ pairs) that is fast at room temperature on the NMR time scale and serves to introduce vertical (dihedral) mirror planes to the molecule.[7b,45] The effective solution symmetry is thus D_{2d} rather than S_4, which makes the two types of equatorial carboxylates equivalent and this predicts the 1:2:1 pattern observed in Figure 2: (a) four axial carboxylates bridging $Mn^{III}\cdots Mn^{IV}$ pairs, (b) four axial carboxylates bridging $Mn^{III}\cdots Mn^{III}$ pairs, and (c) eight equatorial carboxylates bridging $Mn^{III}\cdots Mn^{III}$ pairs. Complex **2** thus retains its overall solution structure, in this solvent at least. The peak assignments were established on the basis of the relative integration ratios and comparisons with the previous spectra of Mn_{12} derivatives possessing other carboxylate groups. Longitudinal (spin−lattice) relaxation times (T_1) were also determined, using the inversion−recovery pulse method (180° − τ − 90°), and are included in Table 3. In general, the T_1 times are all fairly similar: carboxylates bridging $Mn^{III}\cdots Mn^{III}$ pairs have almost identical T_1 times, whereas those bridging $Mn^{III}\cdots Mn^{IV}$ pairs have slightly longer T_1 times. There are too many factors that will influence the T_1 times in such a complicated, polymetallic unit to allow any safe quantitative conclusions, but the longer T_1 times at the $Mn^{III}\cdots Mn^{IV}$ pairs are qualitatively consistent with the stronger antiferromagnetic coupling expected at these bis-oxide-bridged subunits of the structure than at the $Mn^{III}\cdots Mn^{III}$ pairs.

Magnetochemistry

DC Magnetic Susceptibility Studies. Variable-temperature DC magnetic susceptibility (χ_M) data were collected on a microcrystalline powdered sample of **2**, restrained in eicosane to prevent torquing, in a 5.0 kG magnetic field in the 5.0−300 K range. The $\chi_M T$ versus T dependence is similar to those of previously studied $[Mn_{12}O_{12}(O_2CR)_{16}(H_2O)_4]$ complexes, exhibiting a nearly temperature-independent value of 19−20 cm^3 K mol^{-1} in the 150−300 K range which then increases rapidly to a maximum of 51 cm^3 K mol^{-1} at 15 K before decreasing rapidly at lower temperatures. The maximum suggests a large ground-state spin (S) value for the complex of $S = 10$ ($\chi_M T$ = 55 cm^3 K mol^{-1} for $g = 2$), as is expected for an Mn_{12} complex, with the sharp decrease at low temperatures primarily due to a combination of Zeeman and zero-field splitting effects. The ground state and additional data were obtained from a fit of magnetization (M) data collected in the 1.8−4.0 K range in applied DC fields (H) ranging from 1 to 70 kG. The data are plotted in Figure 3 as reduced magnetization ($M/N\mu_B$) versus H/T, where N is Avogadro's number, and μ_B is the Bohr magneton. The $M/N\mu_B$ versus H/T data were fit using the program MAGNET[28] to a model that assumes only that the ground state is populated at these temperatures and magnetic fields, and incorporates isotropic Zeeman interactions, axial zero-field splitting ($D\hat{S}_z^2$) and a full powder average.[46] The best fit is shown as the solid lines in Figure 3, and the fit parameters were $S = 10$, $g = 1.87$, and $D = -0.38$ $cm^{-1} = -0.54$ K. These values are typical for members of the Mn_{12} family. Attempts to fit the magnetization data either with an $S = 9$ or a $S = 11$ ground-state spin gave g/D values of 2.08/−0.47 cm^{-1}

(44) (a) Drago, R. S. *Physical Methods for Chemists*, 2nd ed.; Saunders College: New York, 1992; pp 500−556. (b) La Mar, G. N., Horrocks, W. DeW., Jr., Holm, R. H., Eds. *NMR of Paramagnetic Molecules: Principles and Applications*; Academic Press: New York, 1973. (c) Drago, R. S.; Zink, J. I.; Perry, W. D. *J. Chem. Educ.* **1974**, *51*, 464.

(45) Artus, P.; Christou, G. Manuscript in preparation.

(46) Aliaga-Alcalde, N.; Edwards, R. S.; Hill, S. O.; Wernsdorfer, W.; Folting, K.; Christou, G. *J. Am. Chem. Soc.* **2004**, *126*, 12503.

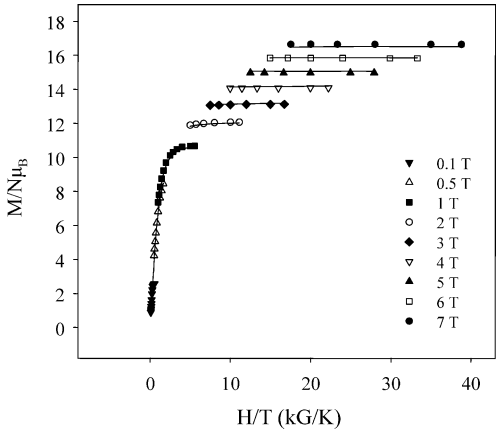

Figure 3. Plot of M/Nμ_B vs H/T for complex **2** at the indicated applied fields. The solid lines are the fit of the data; see the text for the fit parameters.

and 1.71/−0.31 cm^{-1}, respectively. These fits were of comparable quality to that for $S = 10$, but they were rejected on the basis of their unreasonable g values, which should be just slightly less than $g = 2$ for Mn complexes (see also the HFEPR data, vide infra).

To confirm that the obtained D and g parameters for $S = 10$ were the true global rather than a local minimum, and to assess the uncertainty in the obtained g and D values, a root-mean square D vs g error surface for the fit was generated using the program GRID.[28] The error surface (presented in Supporting Information as a 2-D contour plot for the $D = -0.10$ to -0.40 cm^{-1} and $g = 1.8-2.1$ ranges) displays one soft (shallow) fitting minimum. Its lowest error contour describes the region of minimum error spanning $D \approx -0.32$ to -0.44 cm-1 and $g \approx 1.81-1.93$, giving estimated uncertainties in the fit parameters of $D = -0.38 \pm 0.06$ cm^{-1} and $g = 1.87 \pm 0.06$. This level of uncertainty in D (∼16%) is consistent with our general experience that magnetization fits are not the most precise way to measure D values; more precise techniques such as HFEPR are required for more reliable numbers.

AC Magnetic Susceptibility Studies. To probe the magnetization relaxation dynamics and any dependence of the latter on the solvent of crystallization, AC susceptibility data were collected on vacuum-dried, microcrystalline samples of **2** and on wet crystals of **2**·4CH_2Cl_2 in the 1.8−10 K range in a 3.5 G AC field with eight oscillation frequencies (υ) from 5 to 1488 Hz. In Figure 4 are shown the in-phase (χ_M', plotted as $\chi_M'T$) and out-of-phase (χ_M'') AC susceptibility signals for a dried sample of **2**. In an AC susceptibility experiment, a weak field (typically 1−5 G) oscillating at a particular frequency (υ) is applied to a sample. The magnetization vector of the molecule oscillates with the AC field, and there is no out-of-phase AC susceptibility signal (χ_M'') unless the temperature is lowered to a value at which the barrier to magnetization relaxation is comparable to the thermal energy. A frequency-dependent χ_M'' signal is then observed, and there is also a concomitant frequency-dependent decrease in the in-phase (χ_M') signal. A frequency-dependent χ_M'' signal is a necessary but not sufficient[47] indicator of the superparamagnet-like properties of a single-molecule magnet (SMM). The value of $\chi_M'T$ at the lowest temperatures is also especially useful for confirming (or

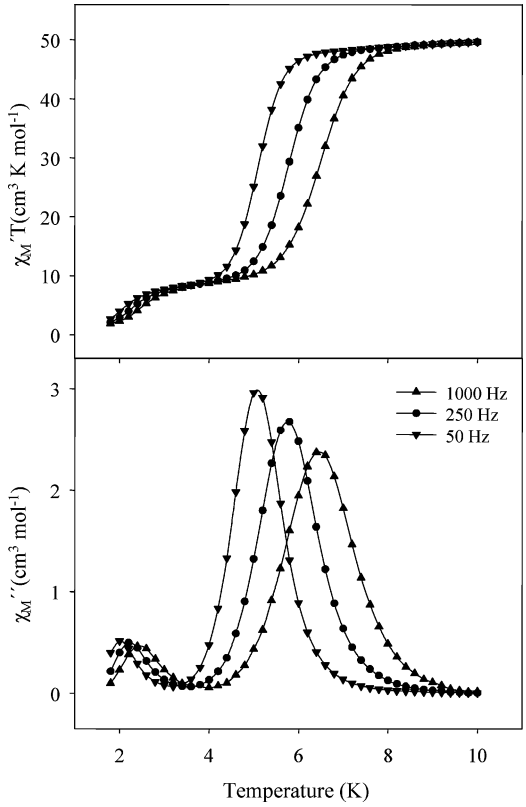

Figure 4. Plot of the in-phase (as $\chi_M'T$) and out-of-phase (χ_M'') AC susceptibility signals vs temperature for dried, microcrystalline complex **2** at the indicated oscillation frequencies.

otherwise) conclusions about the ground-state spin of a molecule determined from DC magnetization fits, avoiding the often complicating effect of the applied DC field and/or low-lying excited states.[48] The $\chi_M'T$ in Figure 4 is ∼50 cm^3 K mol^{-1} above ∼9 K, which is consistent with $S = 10$ and $g \approx 1.90$, in satisfying agreement with the DC magnetization fit parameters. At lower temperatures, there is a frequency-dependent decrease in $\chi_M'T$ and a concomitant increase in χ_M'', indicating that **2** is likely an SMM, as indeed expected for a member of the Mn_{12} family. At still lower temperatures of ∼2.5 K, there is a second feature in both $\chi_M'T$ and χ_M'', indicating the presence of a small fraction of faster-relaxing Mn_{12} species in the sample. This is characteristic of a Jahn−Teller isomer involving an abnormally oriented Mn^{III} JT axis, as mentioned earlier, which results in smaller barriers to magnetization relaxation and thus a faster-relaxing, so-called lower-temperature (LT) form, whose χ_M'' signals are at lower temperatures than the normal, higher-temperature (HT), slower-relaxing form.[40,41]

A comparison of the χ_M'' vs T plots at 1000 Hz for dried and wet (with mother liquor) samples of **2** and **2**·4CH_2Cl_2, respectively, is provided in Figure 5. The dried, microcrystalline sample exhibits two signals, but the wet crystals show only the HT signal. This indicates that the LT signal arises from loss from the crystals of highly volatile CH_2Cl_2 solvent molecules

(47) Chakov, N. E.; Wernsdorfer, W.; Abboud, K. A.; Christou, G. *Inorg. Chem.* **2004**, *43*, 5919.

(48) (a) Soler, M.; Wernsdorfer, W.; Folting, K.; Pink, M.; Christou, G. *J. Am. Chem. Soc.* **2004**, *126*, 2156. (b) Sañudo, E. C.; Wernsdorfer, W; Abboud, K. A.; Christou, G. *Inorg. Chem.* **2004**, *43*, 4137. (c) Murugesu, M.; Habrych, M.; Wernsdorfer, W.; Abboud, K. A.; Christou, G. *J. Am. Chem. Soc.* **2004**, *126*, 4766. (d) Brechin, E. K.; Sañudo, E. C.; Wernsdorfer, W.; Boskovic, C.; Yoo, J.; Hendrickson, D. N.; Yamaguchi, A.; Ishimoto, H.; Concolino, T. E.; Rheingold, A. L.; Christou, G. *Inorg. Chem.* **2005**, *44*, 502.

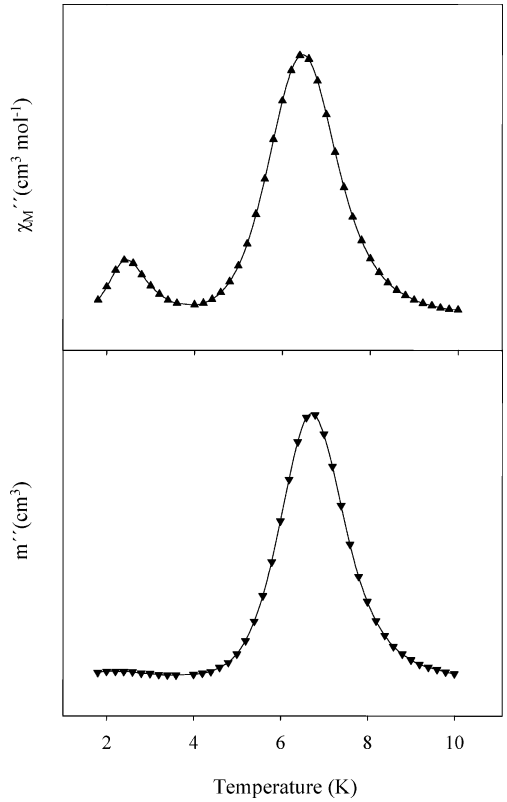

Figure 5. Plot of the out-of-phase AC susceptibility signals vs temperature for dried, microcrystalline complex **2** (top) and for wet crystals of complex **2**·4CH_2Cl_2 (bottom) at 1000 Hz.

and its resulting effect on the crystal lattice and molecular environments. This finding emphasizes the importance of measurements being made on wet crystals whenever possible. Note that the data for wet crystals are plotted as the total out-of-phase susceptibility (m''), since the mass of sample is not known.

The AC susceptibility data as a function of temperature at a constant oscillation frequency (Figures 4 and 5) were supplemented with AC susceptibility data on wet crystals of **2**·4CH_2Cl_2 as a function of AC oscillation frequency at a constant temperature. Such measurements have become a common method of studying the nature of the magnetization relaxation process in SMMs,[34,49,50] as well as spin glasses.[51] The in-phase (as m') and out-of-phase (m'') components of the AC magnetic susceptibility were measured at a fixed temperature of 4.6 K as the AC frequency was varied from 0.1 to 1488 Hz (see Supporting Information). They are also plotted as m' vs m'' (a Cole−Cole or Argand plot) in Figure 6. As with similar measurements on other Mn_{12} complexes,[49,50] the data were best fit to a distribution of single relaxation processes rather than to a single relaxation process. The m' (or χ_M') and m'' (or χ_M'') as a function of angular frequency (ω) for a single relaxation process (i.e. a single relaxation barrier) is given by eqs 3 and 4, respectively, while for a distribution of single relaxation processes (i.e. a distribution of barriers), the m' and m'' behavior is given by eqs 5 and 6, respectively.

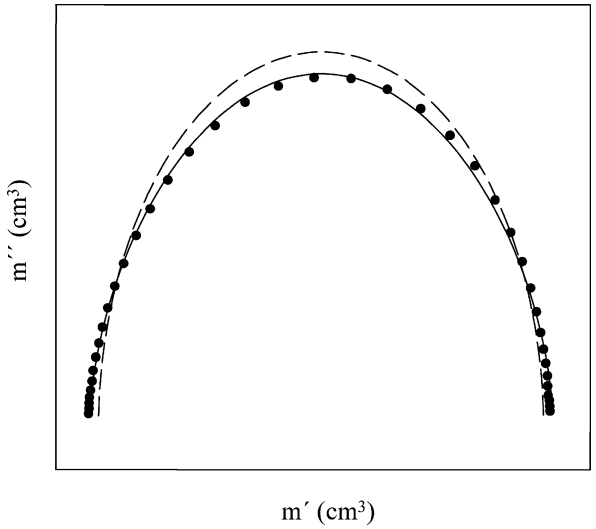

Figure 6. Argand plot of m' vs m'' of wet crystals of **2**·4CH_2Cl_2 at 4.6 K. The dashed line is a least-squares fitting of the data to a single relaxation process as described by eqs 3 and 4. The solid line is a least-squares fitting of the data to a distribution of single relaxation processes as described by eqs 5 and 6.

$$\chi'(\omega) = \chi_s + \frac{(\chi_T - \chi_s)}{1 + \omega^2\tau^2} \tag{3}$$

$$\chi''(\omega) = \frac{(\chi_T - \chi_s)\omega\tau}{1 + \omega^2\tau^2} \tag{4}$$

$$\chi'(\omega) = \chi_s + \frac{(\chi_T - \chi_s)[1 + (\omega\tau)^{1-\alpha}\sin(\alpha\pi/2)]}{1 + 2(\omega\tau)^{1-\alpha}\sin(\alpha\pi/2) + (\omega\tau)^{2(1-\alpha)}} \tag{5}$$

$$\chi''(\omega) = \chi_s + \frac{(\chi_T - \chi_s)(\omega\tau)^{1-\alpha}\cos(\alpha\pi/2)}{1 + 2(\omega\tau)^{1-\alpha}\sin(\alpha\pi/2) + (\omega\tau)^{2(1-\alpha)}} \tag{6}$$

In these equations, χ_s is the adiabatic susceptibility, χ_T is the isothermal susceptibility, $\omega = 2\pi\upsilon$ is the angular frequency, and τ is the magnetization relaxation time. A main objective of such a study is assessing the magnitude of α, a value between 0 and 1, that is included in the expressions for a distribution of single relaxation processes as a gauge of the width of the distribution. The data in Figures 6 and S4 for wet crystals of **2**·4CH_2Cl_2 were least-squares fit to these equations: the fits to eqs 3 and 4 (dashed lines) are clearly inferior to those to eqs 5 and 6 with $\alpha = 0.149$ (solid lines). The relaxation times (τ) obtained from the two fits are very similar, however: $\tau = 0.0393$ s (single relaxation process) and $\tau = 0.0392$ s (distribution of single relaxation processes), with the main difference in the fits arising from the values of the adiabatic and isothermal susceptibility. In addition, the symmetric shape of the Cole−Cole plot confirms a single relaxation process. Hence, the magnetization in **2**·4CH_2Cl_2 relaxes via a single process, and there is a distribution in this single relaxation barrier, the width of which is gauged by the fitting parameter α.

Arrhenius Plot using AC and DC Data. AC susceptibility studies at several oscillation frequencies can be used as a means of determining the effective energy barrier (U_{eff}) to magnetization relaxation, because at the χ_M'' peak maximum the magne-

(49) Aubin, S. M. J.; Sun, Z.; Pardi, L.; Krzystek, J.; Folting, K.; Brunel, L.-C.; Rheingold, A. L.; Christou, G.; Hendrickson, D. N. *Inorg. Chem.* **1999**, *38*, 5329.
(50) Boskovic, C.; Brechin, E. K.; Streib, W. E.; Folting, K.; Bollinger, J. C.; Hendrickson, D. N.; Christou, G. *J. Am. Chem. Soc.* **2002**, *124*, 3725.
(51) (a) Chamberlin, R. V.; Mozurkewich, G.; Orbach, R. *Phys. Rev. Lett.* **1984**, *52*, 867. (b) Weiss, G. H.; Dishon, M.; Long, A. M.; Bendler, J. T.; Jones, A. A.; Inglefield, P. T.; Bandis, A. *Polymer* **1994**, *35*, 1880. (c) Cole, K. S.; Cole, R. H. *J. Chem. Phys.* **1941**, *9*, 341.

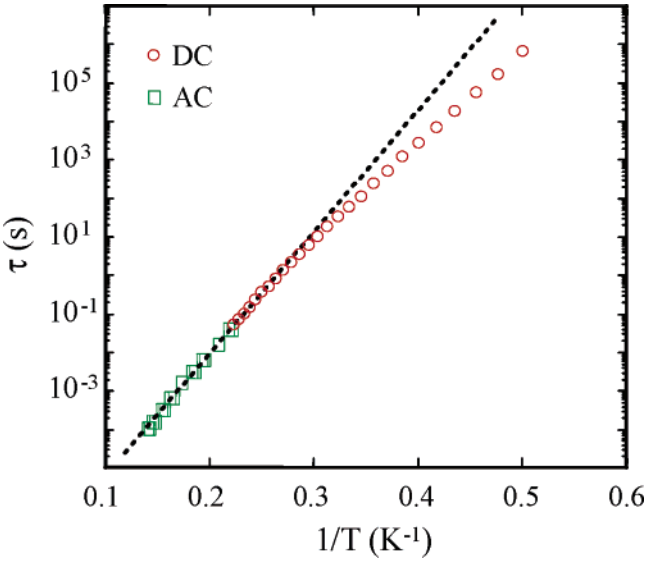

Figure 7. Plot of relaxation time (τ) vs $1/T$ for complex **2** using AC χ_M'' and DC magnetization decay data. The solid line is a fit to the Arrhenius equation. See the text for the fit parameters.

tization relaxation rate ($1/\tau$, where τ is the relaxation time) is equal to the angular frequency ($2\pi\upsilon$) of the AC field. Hence, out-of-phase AC measurements at different oscillation frequencies are a valuable source of rate vs T kinetic data[52] that can be fit to the Arrhenius equation (eq 7)

$$\tau = \tau_0 \exp(U_{eff}/kT) \qquad (7)$$

where U_{eff} is the effective energy barrier to relaxation, k is the Boltzmann constant, and $1/\tau_0$ is the preexponential factor. To supplement these AC data and to provide for a more accurate analysis over a wider range of temperatures, DC magnetization decay data were collected and combined with the AC χ_M'' vs υ data. These data were obtained on a single crystal of **2**·4CH_2Cl_2 using a micro-SQUID apparatus. First, a large DC field of 1.4 T was applied to the sample at ~5 K to saturate its magnetization in one direction, and the temperature was then lowered to a chosen value between 1.3 and 4.4 K. When the temperature was stable, the field was swept from 1.4 to 0 T at a rate of 0.14 T/s, and then the magnetization in zero field was measured as a function of time (see Supporting Information, Figure S5). The combined AC and DC data sets were used to construct the Arrhenius plot of Figure 7. The fit of the thermally activated region above ~3.3 K gave $\tau_0 = 3.3 \times 10^{-9}$ s and $U_{eff} = 74.4$ K. The U_{eff} value is significantly larger than that for Mn_{12}−Ac (60−64 K) and for lower-symmetry Mn_{12} derivatives, and is consistent with the high symmetry of each Mn_{12} molecule in the crystal of **2**. Such larger values of U_{eff} appear typical of high-symmetry Mn_{12} complexes.[36a,c]

Hysteresis Loops. Like all of the reported Mn_{12} derivatives, complex **2** is also expected to be a SMM. This was confirmed by magnetization vs applied DC field sweeps on an aligned single crystal of **2**·4CH_2Cl_2 using a micro-SQUID apparatus. These sweeps exhibited magnetization hysteresis, the diagnostic property of a magnet. The hysteresis loops are presented in Figure 8 and exhibit an increasing coercivity with decreasing

(52) Novak, M. A.; Sessoli, R. In *Quantum Tunneling of Magnetization: QTM '94*; Gunther, L., Barbara, B., Eds.; Kluwer: Amsterdam, 1995; pp 171−188.

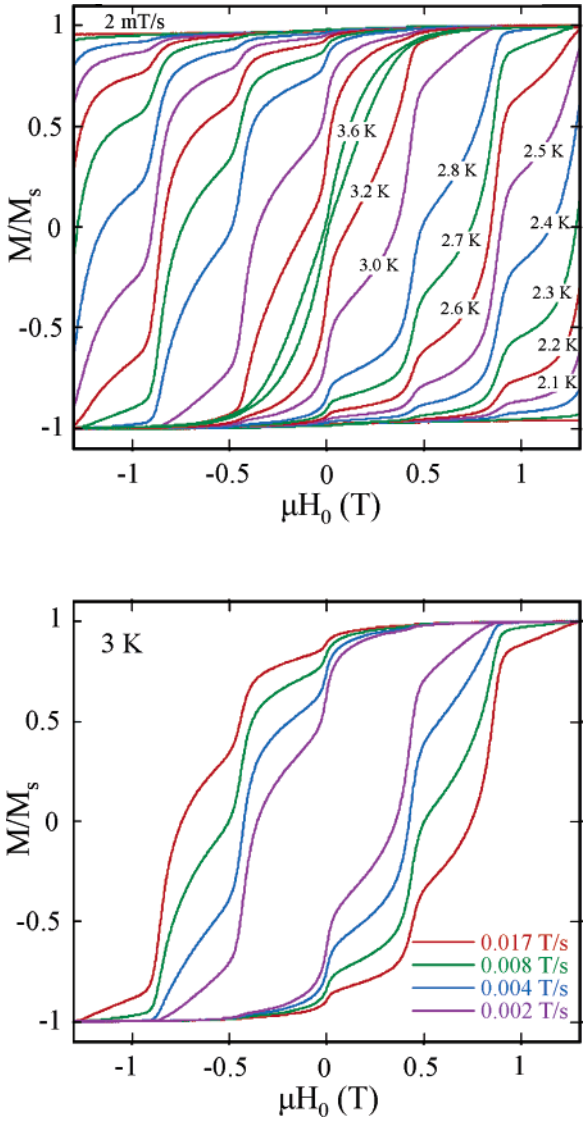

Figure 8. Magnetization hysteresis loops for a single crystal of **2**·4CH_2Cl_2: (top) temperature dependence at a fixed scan rate of 4 mT/s; (bottom) scan-rate dependence at a fixed temperature of 3.0 K. M is normalized to its saturation value, M_s.

temperature and with increasing field sweep rate, as expected for the superparamagnetic properties of a SMM. Hysteresis is observed up to at least 3.6 K at a 2 mT/s sweep rate. In addition, as is usually found for neutral Mn_{12} complexes such as **1** and others, the loops exhibit well-defined steps due to quantum tunneling of magnetization (QTM) at periodic field values. The latter are those at which m_S levels on one side of the potential energy double well of the $S = 10$ ground state are in resonance with m_S levels on the other side, allowing tunneling to occur through the anisotropy barrier. The steps are thus positions of increased magnetization relaxation rate. The separation between steps, ΔH, is proportional to D, as given in eq 8.

$$\Delta H = \frac{|D|}{g\mu_B} \qquad (8)$$

Measurement of the step positions in Figure 8 gave an average ΔH of 0.45 T and thus a $|D|/g$ value of 0.21 cm^{-1} (0.30 K). Assuming $g = 2.0$, this corresponds to a D value of 0.42 cm^{-1} = 0.60 K, consistent with the result of the magnetization vs

field fit on dried samples of **2** ($D = -0.38$ cm^{-1}, $g = 1.87$, $|D|/g = 0.20$ cm^{-1}).

High-Frequency EPR Spectroscopy. HFEPR studies were performed on complex **2**·4CH_2Cl_2 in order to obtain detailed information concerning the spin Hamiltonian and, in particular, to determine the symmetries of the interactions that dominate the QTM behavior. To facilitate comparisons with HFEPR data obtained for the more widely studied SMM, complex **1**,[9−13,53,54] we use the same giant spin approximation (with $S = 10$), resulting in an effective spin Hamiltonian (expanded to fourth order) given in eq 9.

$$\hat{H} \cong \mu_B \vec{B}\cdot\vec{g}\cdot\hat{S} + D\hat{S}_z^2 + B_4^0\hat{O}_4^0 + B_4^4\hat{O}_4^4 \qquad (9)$$

The first term represents the Zeeman interaction due to externally applied magnetic field, where $\vec{g}$ is the Landé *g*-tensor. The second term parametrizes the dominant uniaxial anisotropy with a negative ZFS parameter D (<0). The last two terms, expressed in terms of the Stevens operators $\hat{O}_4^0$ and $\hat{O}_4^4$,[53] represent fourth order ZFS interactions; B_4^0 and B_4^4 denote the corresponding ZFS parameters. We have excluded the second- and fourth-order rhombic ZFS interactions, $E\hat{O}_2^2$ and $B_4^2\hat{O}_4^2$, since they are forbidden in the tetragonal $I4_1/a$ space group. We note that disorder in the hydrogen-bonding can result in a lowering of the local symmetry,[8−15] i.e., one cannot completely ignore the rhombic terms. Indeed, as described earlier, crystals of complex **1** have an intrinsic disorder associated with the $MeCO_2H$ solvate molecules that results in several low-symmetry species, which has a profound influence on the QTM behavior.[12] However, as we shall see, any intrinsic disorder associated with **2**·4CH_2Cl_2 appears to be much weaker than in **1**, consistent with the crystal structure results. At the same time, however, extrinsic disorder caused by loss of volatile CH_2Cl_2 from the crystals can be a lot worse for **2**·4CH_2Cl_2 if the samples are not handled correctly.[13,24,55]

Our previous lower frequency (<80 GHz) studies on **2**·4CH_2Cl_2 confirmed the $S = 10$ ground state, as well as locating a low-lying $S = 9$ state.[13,24] Angle-dependent HFEPR studies for rotations away from the hard plane also suggested that the intrinsic solvent disorder effect found for **1** is absent in **2**·4CH_2Cl_2. Though we were able to obtain reasonable estimates for the axial ZFS parameters from these earlier investigations ($D = -0.456$ cm^{-1} and $B_4^0 = -2.5 \times 10^{-5}$ cm^{-1}), we are now able to report a more precise determination using higher frequencies (up to and above the ZFS energy of the ground to first excited state). Furthermore, angle-dependent HFEPR studies within the hard plane allow us to determine the intrinsic transverse ZFS parameter, B_4^4.[49,11−13]

To accurately determine the uniaxial ZFS parameters, D and B_4^0, the magnetic field was first applied exactly along the easy axis. In this situation, the only off-diagonal terms in eq 9 belong to the $\hat{O}_4^4$ operator [$\equiv (1/2)(\hat{S}_+^4 + \hat{S}_-^4)$]. Owing to the large spin value ($S = 10$), this term affects the low-lying spin states only in very high orders of perturbation theory. Consequently, it can be ignored, resulting in a Hamiltonian which is diagonal in the S_z basis. It is then a simple task to obtain an algebraic expression for the energy eigenvalues, characterized by the quantum number, m_S, which denotes the spin projection onto the molecular easy (*z*) axis (eq 10).

$$E(m_S) = \{D - [30S(S+1) - 25]B_4^0\}m_S^2 + 35B_4^0m_S^4 + \mu_B g_z B m_s \qquad (10)$$

The HFEPR experiment probes the energy differences between eigenstates that differ in m_S by ±1. Thus, a plot of HFEPR data as frequency versus magnetic field gives a series of straight lines with slopes given by $\pm \mu_B g_z/h$ ($\approx \pm$ 28 GHz/T for $g_z = 2$). Such a plot for **2**·4CH_2Cl_2 was obtained (see Supporting Information) and least-squares fit with D, B_4^0, and g_z as the only free parameters (assuming $S = 10$), yielding $D = -0.468(2)$ cm^{-1}, $B_4^0 = -2.5(2) \times 10^{-5}$ cm^{-1}, and $g_z = 1.97(3)$. Using the obtained D and B_4^0 values, one can compute the m_S^2 coefficient in eq 10, which corresponds to the D value obtained from reduced magnetization fits, i.e., $(D - 3275B_4^0) = -0.386$ cm^{-1}. This is in good agreement with the $D = -0.38$ cm^{-1} obtained from the fit of the magnetization data (*vide supra*).

As discussed previously,[11,12] when a strong magnetic field ($B \approx DS/g\mu_B$) is applied in the hard plane, the Zeeman interaction in eq 9 can compete with the uniaxial anisotropy ($D\hat{S}_z^2$). Consequently, terms that were neglected in the *B*//*z* case (i.e.$\hat{O}_4^4$), may now operate in zeroth order, resulting in significant EPR peak position shifts. Thus, by rotating the applied field exactly within the hard plane, one can probe the symmetry of the transverse terms in the spin Hamiltonian.[9,11,12] Figure 9 (top) displays a series of HFEPR spectra, obtained at a frequency of 51.3 GHz and at 15 K, for different field orientations within the hard plane; the angle step is 5°, and the resonances (dips in transmission) have been labeled according to the scheme described elsewhere.[11] Significant shifts in the peak positions can clearly be seen, having a periodicity of 90°, i.e., a four-fold symmetry, which is consistent with the tetragonal $I4_1/a$ space group. The same data are displayed in a color contour plot in Figure 9 (bottom), where the darker shades correspond to stronger EPR absorption; again, the four-fold behavior of the peak position shifts is clearly evident. Superimposed on the data is a single fit to all of the peak positions (gray lines). The fit was performed via exact diagonalization of eq 9, assuming the previously obtained axial ZFS parameters, with B_4^4 and $g_\perp$ ($= g_x = g_y$) as the only free parameters. The fit yields $B_4^4 = \pm 3.0(2) \times 10^{-5}$ cm^{-1} and $g_\perp = 1.94(2)$. Overall, these values are in fair agreement with the ZFS parameters found for **1**,[8−15,53,54] and for another recently discovered high-symmetry Mn_{12} complex, $[Mn_{12}O_{12}(O_2CCH_2Bu^t)_{16}(MeOH)_4]$ (**3**),[13,56] although the D value for **2**·4CH_2Cl_2 is larger by almost 3% compared to **1**. Thus, it would appear that the intrinsic ZFS parameters for high-symmetry Mn_{12} complexes are relatively insensitive to the nature of the ligand. It is therefore surprising that the solvent can have such a dramatic influence on the QTM.[10,12]

It is to be noted that the spectra in Figure 9 are not as sharp as in the earlier experiments.[24] To make direct comparisons, Figure 10 displays spectra obtained for two samples of **2**·

(53) Barra, A. L.; Gatteschi, D.; Sessoli, R. *Phys. Rev. B* **1997**, *56*, 8192.
(54) (a) Hill, S.; Perenbloom, J. A. A. J.; Dalal, N. S.; Hathaway, T.; Stalcup, T.; Brooks, J. S. *Phys. Rev. Lett.* **1998**, *80*, 2453. (b) Perenboom, J. A. A. J.; Brooks, J. S.; Hill, S. Hathaway, T.; Dalal, N. S. *Phys. Rev. B* **1998**, *58*, 330.
(55) del Barco, E.; Kent, A. D.; Chakov, N. E.; Zakharov, L. N.; Rheingold, A. L.; Hendrickson, D. N.; Christou, G. *Phys. Rev. B* **2004**, *69*, 020411.
(56) Hill, S.; Anderson, N.; Wilson, A.; Takahashi, S.; Chakov, N. E.; Murugesu, M.; North, J. M.; Dalal, N. S.; Christou, G. *J. Appl. Phys.* **2005**, *97*, 10M510.

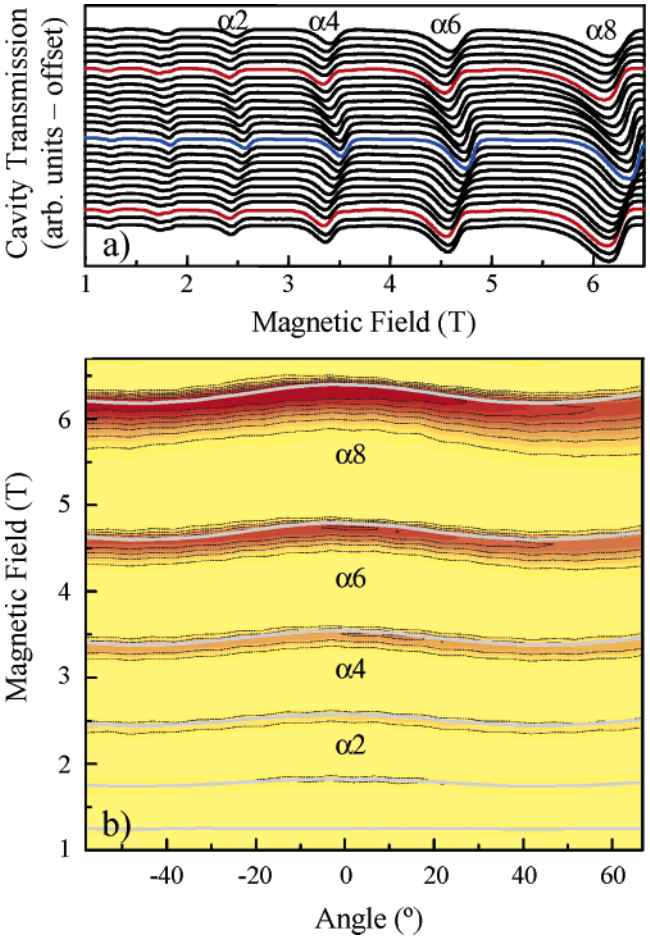

Figure 9. (a) HFEPR spectra (signal transmitted through the cavity) obtained at different field orientations within the hard plane. The angle step is 5°, the frequency is 51.3 GHz, and the temperature is 15 K. The resonances have been labeled according to ref 10. The blue trace corresponds to the field oriented parallel to one of the short square edges of the crystal; the red traces are 45° to either side of this orientation. A four-fold shift in the peak positions is clearly evident. (b) Color contour plot of the data in (a), where the darker shades correspond to stronger EPR absorption. Superimposed on the data is a single fit to all of the peak positions (gray lines).

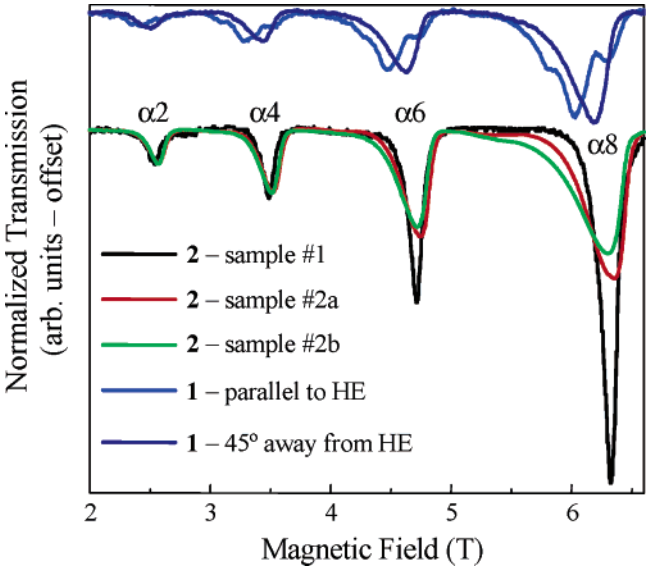

Figure 10. A comparison between hard plane EPR spectra obtained at 51.4 ± 0.1 GHz and 15 K for two samples of **2** and a single sample of **1**. The spectra of **2** were all obtained with the field parallel to one of the short square edges of the crystal (blue trace in Figure 15a), and the data have been normalized according to the α2 peak intensity (see also main text). The dark blue trace of **1** was obtained with the magnetic field applied parallel to the hard (HE) axis associated with the low-symmetry disordered species, resulting in the resolution of shoulders on the high- and low-field sides of the main peak. The light blue trace of **1** was obtained with the magnetic field applied at 45° to the HE axis (within the hard plane), resulting in the observation of only a single peak.[9,10,12] The fact that the light-blue peak of **1** is observed at a slightly lower field than the peaks of **2** is a direct confirmation of the slightly larger *D* value for complex **2**.

$4CH_2Cl_2$ and for a single sample of **1**. All of the data were obtained at 15 K and at a frequency of 51.4 ± 0.1 GHz, with the field applied within the hard plane. The samples of **2**·$4CH_2Cl_2$ were prepared in separate syntheses, approximately 1 year apart. Extreme care was exercised in cooling the sample of **1** and the sample #1 of **2**·$4CH_2Cl_2$, as described in the Experimental Section. The sample #2 of **2**·$4CH_2Cl_2$ was also handled with the same care upon its first cooling (#2a), and then subsequently cycled to room temperature under vacuum before re-cooling (#2b). It is clear from Figure 10 that the line widths of the highest field EPR peaks differ considerably for the three different runs of **2**. The spectra have been normalized according to the α2 peak intensity, which is less sensitive to the effects of distributions in the ZFS parameters.[18−20] Even though this normalization leads to significant differences in the heights of the α6 and α8 peaks, the integrated area under each peak is the same for each run (to within a 10% random error), as expected for experimental conditions which were nominally identical for the three runs.

The broader EPR peaks indicate distributions in the ZFS parameters − in other words, disorder. We believe that the greater disorder associated with sample #2 of **2** is caused by solvent loss, and possibly also to microcracking. The solvent loss is evident from the fact that the thermally cycled sample exhibits broader EPR peaks, and also from the fact that the out-of-phase AC susceptibility data on dried microcrystals indicate the presence of a significant fraction of faster-relaxing Mn_{12} species, whereas this is not evident from the AC data obtained from wet crystals (Figure 5). The HFEPR data for sample #1 of **2**·$4CH_2Cl_2$ indicate almost no disorder, i.e., the line shapes are approximately Lorentzian and symmetric, and the line widths (full-width-at-half-maximum, fwhm) are more-or-less identical for each peak: α8 = 0.14 T, α6 = 0.13 T, α2 = 0.12 T. In contrast, the fwhm for sample #2 are strongly peak dependent: α8 = 0.34 T, α6 = 0.23 T, α2 = 0.18 T for #2a; and α8 = 0.40 T, α6 = 0.26 T, α2 = 0.18 T for #2b. This behavior is a clear sign of *D* and *E* strain,[18−20] although it is not so obvious which effect is dominant (see below).

It could be argued that the slight disorder in a few bound $BrCH_2CO_2^-$ ligands and the solvate CH_2Cl_2 groups seen in the X-ray analysis will yield a distribution of molecular species ("isomers") in the crystal and a resulting distribution of local symmetries, but the fact that sample #1 exhibits almost no measurable *D* or *E* strain suggests that intrinsic ligand and solvate disorder has no significant effect on the spin Hamiltonian. Remember also that there are four CH_2Cl_2 molecules per Mn_{12}, a full complement allowing weak hydrogen-bonding with each of the four bound water molecules, which thus does not represent a significant symmetry-lowering perturbation of the Mn_{12} molecule, in contrast to the situation in **1**.[8] For these reasons, it is concluded that complex **2**·$4CH_2Cl_2$ represents a particularly attractive alternative to **1** for studying the quantum

dynamics of giant spin molecules with high symmetry, since the symmetry of the QTM should be dominated by the intrinsic symmetry of the molecule.

However, we stress again that not all samples yield the same high-quality data. The cause of the poorer data for sample #2 is not entirely clear, although the quality of its surface was visibly worse than that of sample #1. Nevertheless, it is also possible that sample #2 lost solvent during the first cooling, despite the various measures taken to avoid this. CH_2Cl_2 is a volatile solvent, and crystals of **2**·4CH_2Cl_2 are far more susceptible to solvent loss than **1**.[13,20,46] Upon comparing the data in Figure 10 for sample #2 of **2** with those of sample #1, it is evident that intensity transfers from the centers of the EPR peaks mainly to the low-field tails. A similar behavior has also been observed in **1** (in addition to the *E*-strain) which can be explained by easy-axis tilting.[11] We speculate that the loss of CH_2Cl_2 solvent from **2**·4CH_2Cl_2 leads to a loss of crystallinity, giving a significant random distribution of the orientations of the molecular *z*-axes. Such a distribution of *z*-axes has also been noted by del Barco et al.[55]

Finally, we emphasize that the disorder implied by the data for Mn_{12}−BrAc (**2**) in Figure 10 is quite different from the discrete intrinsic disorder found for Mn_{12}−Ac (**1**), which has nonvolatile solvate molecules and whose EPR line shapes are quite reproducible.[9,11−13] Furthermore, for **1** the line widths and shapes exhibit a pronounced dependence on the field orientation within the hard plane, revealing the different symmetries of the constituent isomers in the crystal. For reference, the two uppermost spectra in Figure 10 were obtained for **1** with the field applied at two different orientations within the hard plane. In one case, the resonances exhibit three distinct peaks; in the other case, the three peaks collapse into a single broad asymmetric peak (see caption and refs. **11**−**13** for further explanation). No such behavior is seen in Figure 9 (top) for **2**·4CH_2Cl_2 (i.e. the line widths do not vary with field orientation), implying that the disorder which causes the line broadening is completely random, reaffirming our assertion that the disorder in sample #2 is due to solvent loss and not to any intrinsic ligand or solvent disorder. Overall, the line shape associated with the disordered sample #2 of **2**·4CH_2Cl_2 is quite similar to that of the darker blue peaks of **1**. This would imply relatively weak *E*-strain compared to the low-symmetry species of **1**, which possess *E* values on the order of 0.014 cm^{-1}.[12] Therefore, the main result of the disorder is likely *D* strain and easy-axis tilting. In view of this disorder, the ZFS parameters quoted above correspond to the mode of the distribution.

^{55}Mn NMR Spectroscopy. There has been great interest recently in using solid-state ^{55}Mn NMR studies to learn more about Mn_{12} SMMs,[25,57−59] particularly at extremely low temperatures where thermal fluctuations are of diminishing importance and quantum effects take over.[60,61] This work has mainly concentrated on the Mn_{12}−Ac complex **1**. Most of these studies have taken advantage of the ability of ^{55}Mn NMR spectroscopy to probe individual symmetry-equivalent groups of Mn sites, whereas other techniques such as EPR can only probe the complete molecule. Thus, these previous NMR studies have established that there are three symmetry types of Mn within **1**,[25,57] the central group of 4 Mn^{IV} ions and two groups of 4 Mn^{III} outer ions, as expected under S_4 symmetry. In addition, the sensitivity of the NMR signals to external magnetic fields has provided support for the spin structure of the molecule leading to the $S = 10$ ground state, namely that the spins of the central 4 Mn^{IV} ions (each $S = {}^3/_2$) are aligned antiparallel to those of the outer 8 Mn^{III} ions (each $S = 2$), giving a molecular ground state of $S = 16 - 6 = 10$.[57−59] Further, ^{55}Mn NMR studies on **1** have also been employed to probe QTM within this complex;[58−61] in particular, ultralow temperature (down to 20 mK) spin−lattice relaxation time (T_1) data on an oriented microcrystalline powder of **1** were obtained by Morello et al.[60,61] Below 800 mK, they report an essentially temperature-independent T_1 region and conclude that relaxation in this region occurs only through QTM, driven by the significant number (∼5%) of faster-relaxing Mn_{12} molecules located throughout the crystals of **1** and which serve as relaxation sources.

With the availability of the superior crystals of **2**·4CH_2Cl_2 compared with that of **1**, we decided to carry out a full investigation of the former by ^{55}Mn NMR spectroscopy. Our general aims were several, including to assess the degree to which the available NMR data on **1** are compromised by the mixture of isomers of various symmetries present in its crystals, and to thus determine the NMR data for truly axially symmetric Mn_{12}. In addition, we also wished to assess the influence of solvent loss from **2**·4CH_2Cl_2 on the observed NMR spectra, and to thus determine the extent to which ^{55}Mn NMR might be useful as a probe of solvent-induced changes to the local symmetry at a Mn_{12} molecule; this would also complement the HFEPR studies and their conclusions on these points described above. A more specific aim of our study was the following: wet crystals of **2**·4CH_2Cl_2 do not contain significant amounts of a faster-relaxing species (i.e., the abnormal JT isomer), and thus we argued that the data from a T_1 study would be of interest for comparisons with the data and conclusions of Morello et al. In fact, we hypothesized that presumably T_1 times should consequently be longer than those for **1**, and not dominated by QTM.

The ^{55}Mn NMR studies were carried out in 365 mK to 3 K range. Figure 11 (a and b) shows a comparison of the NMR spectra from a single crystal and an aligned microcrystalline powder of **2**·4CH_2Cl_2 obtained in the absence of an applied magnetic field. The spectra consist of three groups of NMR peaks, labeled Mn(3), Mn(2), and Mn (1), in accordance with the labeling scheme of Figure 1. The single-crystal spectrum is much sharper and better resolved, showing structural features that are not observed in the powder spectrum, especially the well-defined quadrupolar splitting of the second peak into a quintet due to the ^{55}Mn nuclear spin of $I = {}^5/_2$ (100% natural abundance). Indeed, a major finding of this NMR study is that the standard practice of preparing aligned, microcrystalline powder samples of Mn_{12} compounds produces results significantly different from those of a single crystal, both in the resolution and peak position.[25] Grinding-induced heat must cause a greater possibility for solvent loss or other structural damage which in turn gives a distribution of Mn_{12} microenvironments.

(57) Kubo, T.; Goto, T.; Koshiba, T.; Takeda, K.; Awaga, K. *Phys. Rev. B* **2002**, *65*, 224425.
(58) Lascialfari, A.; Jang, Z. H.; Borsa, F.; Carretta, P.; Gatteschi, D. *Phys. Rev. Lett.* **1998**, *81*, 3773.
(59) Furukawa, Y.; Watanabe, K.; Kumagai, K.; Borsa, F.; Gatteschi, D. *Phys. Rev. B* **2001**, *64*, 104401.
(60) Morello, A.; Bakharev, O. N.; Brom, H. B.; Sessoli, R.; de Jongh, L. J. *Phys. Rev. Lett.* **2004**, *93*, 197202.
(61) (a) Morello, A.; Bakharev, O. N.; Brom, H. B.; de Jongh, L. J. *Polyhedron* **2003**, *22*, 1745. (b) Morello, A.; Bakharev, O. N.; Brom, H. B.; de Jongh, L. J. *J. Magn. Magn. Mater.* **2004**, *272*, 1015.

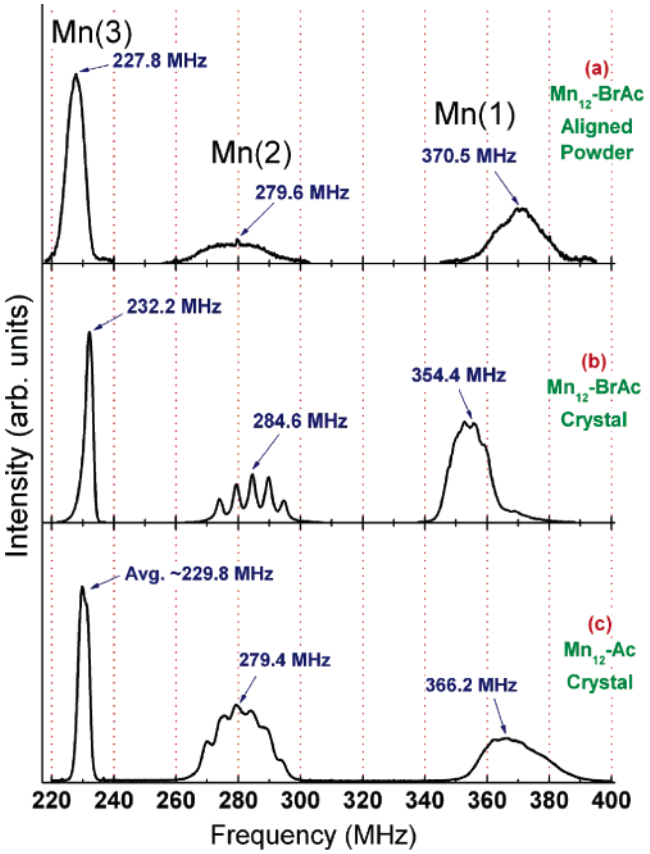

Figure 11. Comparison of single crystal (bottom) and powder (top) NMR spectra taken below 2 K in zero external field. Frequency shifts and broadening in powdered sample likely due to intense pressure and heat induced by crushing sample.

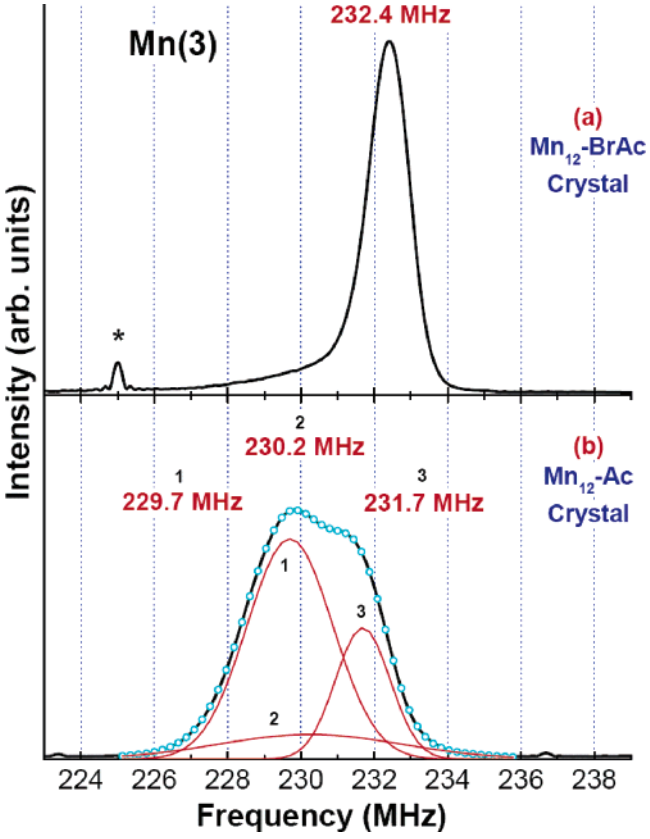

Figure 12. Comparison of the Mn^{4+}, Mn(3), signals for (a) Mn_{12}−BrAc and (b) Mn_{12}−Ac. The peaks for Mn_{12}−Ac can be simulated by using three Gaussian components, as shown in (b). This is evidence for at least three structural variants in the Mn_{12}−Ac crystal lattice. * denotes noise from outside source.

We note that the earlier NMR work on the Mn_{12} and Fe_8 SMMs had been carried out on magnetically aligned microcrystalline powders, because of the lack of large enough single crystals,[57−61] and must thus be interpreted with this reservation.

Peak assignments are as previously discussed:[25,57] Mn(3), at 232.2 MHz is from the 4 Mn^{IV} central ions, which are in a cubic environment as evidenced by the lack of quadrupolar splitting. The second peak, Mn(2), at 284.6 MHz is from one group of 4 Mn^{III} outer ions, and the third peak at 354.4 MHz is from the other group, Mn(1). Mn(2) is distinguished by its smaller tipping angle, $\theta = 7.9°$, of the local JT (z) axis to the Mn_{12} easy-axis (cell c-axis), whereas the Mn(1) group has a tipping angle of $\theta = 34.0°$. This canting away from the c-axis is also responsible for the larger quadrupolar splitting of the second peak and for the higher resonance frequency of third peak. The hyperfine field at each site is calculated by simply taking the central resonance frequency of each peak and dividing by the gyromagnetic ratio of ^{55}Mn, $\gamma/2\pi = 10.5$ MHz/T. The Mn(3) peak (Mn^{IV}, $\theta = 0$), Mn(2) peak (Mn^{3+}, $\theta = 7.9°$), and Mn(1) peak (Mn^{3+}, $\theta = 34.0°$) have hyperfine fields of 22.11, 26.63, and 33.75 T, respectively. As shown elsewhere,[25] these angles and the quadrupolar splittings can be used to calculate the quadrupolar coupling parameter (e^2qQ). Peaks Mn(2) and Mn(1) have e^2qQ values of 35.33 ± 0.35 and 41.43 ± 1.26 MHz, respectively, which can be compared with the corresponding values of 30.6 ± 0.7 and 40.6 ± 1.5 MHz for Mn_{12}−Ac (**1**).[57]

Since powdering the sample has such a large effect on the NMR spectrum of Mn_{12}−BrAc (**2**), we also examined the NMR spectrum of a single crystal of Mn_{12}−Ac (**1**), and this is shown in Figure 11c. The resolution is clearly poorer than that for a single crystal of **2**·4CH_2Cl_2. Kubo et al.[57] had used magnetically aligned powder of Mn_{12}−Ac and reported results similar to those discussed here, specifically, three groups of peaks centered at 230.2, 279.4, and 364.4 MHz, apparently with poorly resolved quadrupolar splitting on all three peaks. Figure 12 shows an expansion for better comparison of the Mn(3) peak for single crystals of Mn_{12}−BrAc and Mn_{12}−Ac. The peak for Mn_{12}−Ac is much broader than that for Mn_{12}−BrAc and shows unresolved features previously assigned to quadrupolar splitting; however, this would also be expected for the Mn_{12}−BrAc peak, and the lack of quadrupolar splitting for the latter thus suggests the structure of the Mn(3) peak of Mn_{12}−Ac is instead due to the different hydrogen-bonded isomers mentioned earlier.

It should be noted that the Mn(3) peak for the single crystal of Mn_{12}−Ac is actually slightly broader than that reported for a powdered sample of this compound.[57] We attribute this counterintuitive observation to the fact that powdering of Mn_{12}−Ac crystals artificially narrows the Mn(3) line by perturbing the environments of all molecules and thus decreases the differences between the various isomers present. The Mn(2) signal clearly shows six peaks, which we consider as conclusive verification of the presence of isomers. The Mn(3) peak of the single-crystal spectrum of Mn_{12}−Ac in Figure 12b was simulated as three overlapping isomer signals, as shown. Calculation of their internal fields gives 21.89, 21.93, and 22.07 T, respectively, compared with 21.8 T reported by Kubo et al.[57]

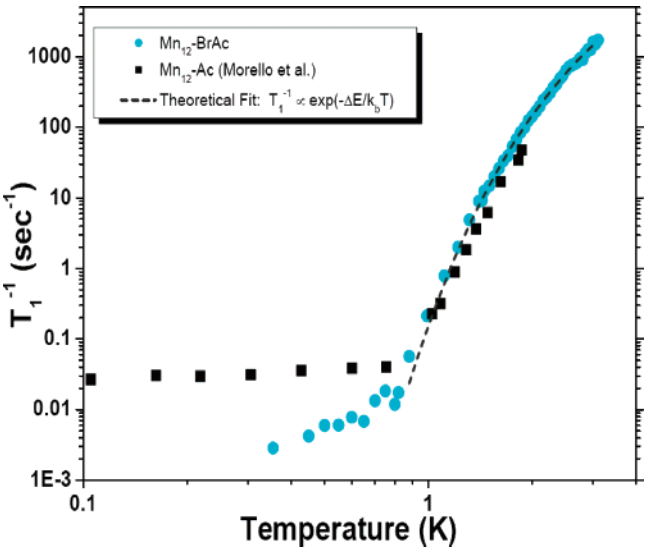

Figure 13. Temperature dependence of T_1^{-1} for Mn_{12}−Ac and Mn_{12}−Ac.[60] The dashed line is the fit of the high-temperature data (>1 K) for Mn_{12}−BrAc; see the text for the fit parameters.

Overall it is clear from Figure 12a that the lack of isomers present in Mn_{12}−BrAc and the resulting very narrow peak as compared with Mn_{12}−Ac shows that Mn_{12}−BrAc is a more homogeneous system to study and is the thus a benchmark with which other Mn_{12} SMMs should be compared.

***T_1* Studies.** The first peak of Figure 11b has a central frequency of 232.2 MHz and a full-width-at-half-height (fwhh) of ~3.5 MHz. To saturate such a wide resonance, a modified comb pulse was used. The comb contained a series of four $\pi/2$ pulses at different frequencies about the center of the line and was repeated 25 times to saturate the central spectral region. This method proved effective in ensuring saturation of all nuclear transitions, as evidenced by the good fits of the data to a single exponential.[59,62] Morello et al. had earlier used the Master Equation to fit their T_1 data. [60,61] Such an approach is appropriate if the system exhibits quadrupolar splitting and the satellites contribute to the relaxation of the nuclei. It should be noted that there is no evidence for quadrupolar splitting in the Mn(3) peak of Mn_{12}−BrAc; therefore, a multiexponential recovery defined by the Master Equation is not appropriate.

T_1 values were obtained from a fit of the data to eq 11,

$$M(t) = (M_\infty - M_0)[1 - \exp(-t/T_1)] + M_0 \qquad (11)$$

where $M(t)$ is the time-dependent nuclear magnetization, M_∞ is the equilibrium magnetization, t is the time between the saturation sequence and the observation spin−echo, M_0 is the remnant magnetization immediately following the saturation comb, and T_1 is the longitudinal (spin−lattice) relaxation time. A log plot of T_1^{-1} vs T is shown in Figure 13, which also includes the corresponding literature results for the aligned powder of Mn_{12}−Ac.[60] At high temperatures (>1 K), the data for the two systems correlate reasonably well. Below 1 K, however, the Mn_{12}−BrAc relaxation rate is roughly an order of magnitude smaller than that for Mn_{12}−Ac.

A standard high-temperature analysis[58,60−62] was performed for the data over the 1−3 K range, which involves fitting these data to a model whereby thermal fluctuations induce a transition from the $m_S = \pm 10$ ground state to an excited state, providing an appropriate transverse field to relax the nuclei. This transverse field is supplied through the contact hyperfine interaction. Energy levels with $m_S \geq \pm 8$ were not considered in the following fits since their population is negligible at these temperatures. The time-correlation function for the induced transverse field, $\langle h_\perp^2 \rangle$, is given in eq 12,

$$\langle h_\perp(0) h_\perp(t) \rangle = \langle h_\perp^2 \rangle \exp(-t/\tau) \qquad (12)$$

where τ is the fluctuation correlation time.

In the high-temperature limit (>1 K), $\tau \approx \tau_0 \exp(\Delta E/kT)$, where ΔE is the level splitting between the $m_S = \pm 10$ and $m_S = \pm 9$ states. This splitting has been measured to be 10.02 cm^{-1} (14.41 K) by frequency-swept microwave resonance experiments.[63] Assuming $\omega_N^2 \tau^2 \gg 1$, we get eq 13

$$T_1^{-1} = C \exp(-\Delta E/k_b T) \qquad (13)$$

where C is expanded in eq 14;

$$C = \frac{\gamma_N^2 \langle h_\perp^2 \rangle}{\omega_N^2 \tau_0} \qquad (14)$$

$\omega_N^2 = 2.13 \times 10^{18}$ rad^2/s^2 is the angular frequency squared and $\gamma_N^2 = 4.35 \times 10^{15}$ $rad^2\ s^2\ T^{-2}$ is the gyromagnetic ratio squared. The fit of the data to eq 13 gives $C = 1.43 \times 10^5$ rad/s and $\Delta E = 13.7$ K when both parameters were allowed to vary freely. Using this C value, we calculate $\langle h_\perp^2 \rangle / \tau_0 \approx 7.0 \times 10^7$ (T^2/s), in agreement with the earlier reported value of 4.5×10^7 (T^2/s) for Mn_{12}−Ac.[59,61] The obtained value of $\Delta E = 13.7$ K is comparable to the directly measured value of 14.41 K for Mn_{12}−Ac at 2.56 K, showing some increase with decreasing temperature.[63] Of greater interest is the data below 1 K, where it had been previously reported for Mn_{12}−Ac that an additional mechanism for longitudinal relaxation is important.[60,61] This relaxation mechanism has been ascribed to QTM in zero-field and is thus temperature independent. From Figure 13, it is apparent that at ~0.8 K the data for Mn_{12}−BrAc begin to deviate from the higher-temperature fit, suggesting a new mechanism for T_1 relaxation. Surprisingly, at 0.365 K the relaxation rate (T_1^{-1}) for Mn_{12}−BrAc differed (was slower) by roughly an order of magnitude than that for Mn_{12}−Ac and had not reached a temperature-independent region, in contrast to the Mn_{12}−Ac data. Two mechanisms are clearly responsible for the relaxation of the nuclear spins over the measured temperature range. The tail below 0.800 K could be well fit to a T^α behavior with $\alpha \approx 2$. Further studies at lower temperatures are necessary and planned for additional insight into the T_1 mechanism below 0.800 K.

Conclusions

Both Mn_{12}−Ac **(1)** and Mn_{12}−BrAc **(2)** crystallize in a tetragonal space group with the Mn_{12} molecule lying on an S_4 symmetry element, but the data for the former complex are significantly compromised by the mixture of isomers in the crystal. In contrast, a crystal of complex **2** is much closer to an ideal

(62) Fukushima, E.; Roeder, S. B. W. *Experimental Pulse NMR: A Nuts and Bolts Approach*; Perseus Books: Jackson, TN, 1981.

(63) Mukhin, A. A.; Travkin, V. D.; Zvezdin, A. K.; Lebedev, S. P.; Caneschi, A.; Gatteschi, D. *Europhys. Lett.* **1998**, *44*, 778.

situation of a three-dimensional ensemble of identical, monodisperse molecular particles in identical environments. This is clearly apparent in the both the EPR and NMR spectroscopic studies we have described. It should be noted that the use of single crystals of both compounds in both studies precludes the possibility that differences in the means of preparation and the particle sizes of a microcrystalline powder are the cause of the discrepancies.

The magnetization studies establish that **2** has the usual $S = 10$ ground state of a normal Mn_{12} SMM. It exhibits the frequency-dependent out-of-phase AC susceptibility signals that are suggestive of a SMM, and the hysteresis loops in magnetization vs applied DC field sweeps that are the diagnostic, confirmatory property of a magnet. In this regard, **2** is the same as **1**, but comparison of the spectroscopic signatures of the two complexes then reveals major differences. Detailed analysis of the HFEPR spectra for **2**·$4CH_2Cl_2$ reveals ZFS parameters very similar to those of **1** but with no evidence for the discrete hydrogen-bonding-induced disorder that results in the multiple isomers found in **1** and which causes significant inhomogeneous broadening of the EPR signals. This is due to the full complement of four CH_2Cl_2 molecules in **2**. The volatility of CH_2Cl_2 means that solvent loss from the crystals is more of a problem for **2** than for **1** and that crystals must be treated carefully in preparation for experiments; however, this is a small price to pay because crystals of **2** that have not been damaged by solvent loss are intrinsically far cleaner than comparable samples of **1**, giving rise to HFEPR spectra that show almost no measurable distributions. This suggests that future investigations of **2** could lead to important new insights into the quantum magnetization dynamics of giant spin molecules, which may ultimately enable us to also improve our knowledge of decoherence in such molecules.

Similar conclusions also result from the single-crystal ^{55}Mn NMR studies that clearly support the magnetization and EPR data in concluding that Mn_{12}−BrAc is a model Mn_{12} system to study. The use of a far "cleaner" crystal than is possible for **1**, in combination with the single-crystal nature of the described NMR experiments, has allowed for enhanced resolution in the resulting spectra, which has also allowed us to obtain important information (such as quadrupole splittings) that might otherwise be lost through the process of crushing the sample or obscured by overlap of the signals of multiple isomers. In addition, spin−lattice relaxation measurements show almost an order of magnitude difference with those of Mn_{12}−Ac and show no sign of becoming constant, an observation under continuing investigation. Finally, the power of NMR to probe individual symmetry subsets of Mn atoms within the core has allowed the fine structure on the Mn^{IV} peak in **1** to be assigned to the isomers, since quadrupolar splitting is not expected for isotropic Mn^{IV}. Indeed, such a use of Mn NMR in other Mn^{IV}-containing clusters may well be a useful new avenue to explore for studying other types of SMMs.

Finally, we note that the less inhomogeneous broadening of EPR and NMR spectra not only allows for higher precision experiments but may also pave the way for more systematic investigations of QTM in SMMs and may even enable observation of new phenomena such as quantum interference effects caused by higher-order (>second-order) transverse terms in the spin Hamiltonian.

Acknowledgment. This work was supported by the National Science Foundation (Grants CHE-0414155 and DMR-0506946). We thank Dr. Michael Hoch for helpful discussions.

Supporting Information Available: X-ray crystallographic files in CIF format for complex **2**·$4CH_2Cl_2$. This material is available free of charge via the Internet at http://pubs.acs.org.

JA060796N